Phase-space structures II: Hierarchical Structure Finder

M. Maciejewski[1,2], S. Colombi[1], V. Springel[2], C. Alard[1], F.R. Bouchet[1]*

[1] *Institut d'Astrophysique de Paris, CNRS UMR 7095 & UPMC, 98 bis boulevard Arago, 75014 Paris, France*
[2] *Max-Planck-Institut für Astrophysik, Garching, Karl-Schwarzschild-Straße 1, 85741 Garching bei München, Germany*

1 December 2008

ABSTRACT

A new multi-dimensional Hierarchical Structure Finder (HSF) to study the phase-space structure of dark matter in N-body cosmological simulations is presented. The algorithm depends mainly on two parameters, which control the level of connectivity of the detected structures and their significance compared to Poisson noise. By working in 6D phase-space, where contrasts are much more pronounced than in 3D position space, our HSF algorithm is capable of detecting subhaloes including their tidal tails, and can recognise other phase-space structures such as pure streams and candidate caustics.

If an additional unbinding criterion is added, the algorithm can be used as a self-consistent halo and subhalo finder. As a test, we apply it to a large halo of the Millennium Simulation, where 19% of the halo mass are found to belong to bound substructures, which is more than what is detected with conventional 3D substructure finders, and an additional $23 - 36\%$ of the total mass belongs to unbound HSF structures. The distribution of identified phase-space density peaks is clearly bimodal: high peaks are dominated by the bound structures and show a small spread in their height distribution; low peaks belong mostly to tidal streams, as expected. However, the projected (3D) density distribution of the structures shows that some of the streams can have comparable density to the bound structures in position space.

In order to better understand what HSF provides, we examine the time evolution of structures, based on the merger tree history. Given the resolution limit of the Millennium Simulation, bound structures typically make only up to 6 orbits inside the main halo. The number of orbits scales approximately linearly with the redshift corresponding to the moment of merging of the structures with the halo. At fixed redshift, the larger the initial mass of the structure which enters the main halo, the faster it loses mass. The difference in the mass loss rate between the largest structures and the smallest ones can reach up to 20%. Still, HSF can identify at the present time at least 80% of the original content of structures with a redshift of infall as high as $z \leq 0.3$, which illustrates the significant power of this tool to perform dynamical analyses in phase-space.

Key words: methods: data analysis, methods: numerical, galaxies: haloes, galaxies: structure, cosmology: dark matter

1 INTRODUCTION

When Zwicky (1933) studied galaxy velocities in clusters, he was the first to notice that there should be about one order of magnitude more matter in the universe than the observed amount of baryonic matter to explain the proper motions of galaxies through gravitational forces. Dark Matter (DM) was introduced to overcome this problem. Later on, the existence of a dark matter component

was confirmed by the analysis of galaxy rotation curves (Rubin & Ford 1970). Recent studies of gravitational lensing (e.g. Van Waerbeke et al. 2000) and, more generally, multiwavelength observations in e.g. the COSMOS project (Massey et al. 2007) provide additional proofs for the existence of DM. Other constraints on the non-baryonic nature of DM were also set by the analysis of the Cosmic Microwave Background (e.g. Hinshaw et al. 2008).

For the last three decades, the DM paradigm has been studied extensively in the context of cosmological N-body simulations. The comparison of structures formed in such simulations to observed ones excluded some of the theo-

* E-mail: maciejewski.michal@gmail.com; colombi@iap.fr; volker@mpa-garching.mpg.de; alard@iap.fr; bouchet@iap.fr

retical models, such as Hot Dark Matter and led to the nowadays commonly accepted Λ-Cold Dark Matter (ΛCDM) model. In the ΛCDM model, dark matter is collisionless, with a very small velocity dispersion at high redshift; structures are built in a hierarchical, bottom-up process, where small structures arise first, seeded from initial fluctuations, and then merge together to build up larger and larger structures, designated commonly as *haloes*. Inside the gravitational wells of these dark matter haloes, baryonic matter forms galaxies (White & Rees 1979).

Recently, the efforts to finally identify the physical nature of dark matter particles, either directly through detecting them in ground-based dark matter particle detectors or indirectly by observing their annihilation radiation, have intensified. At the same time, the ever increasing resolution of N-body simulations (e.g. Springel et al. 2008) puts new levels of demand on the field of theoretical study of non-linear halos. The careful analysis of cosmological structures moves from the study of spherically averaged three-dimensional density profiles (Navarro, Frenk & White 1997) to the study of the full six dimensional phase-space. For example, this concerns the analyses of the properties of caustics described analytically in e.g. Bertschinger's secondary infall model (Bertschinger 1985) and recently reviewed in the context of numerical simulations (Mohayaee & Salati 2008; White & Vogelsberger 2008). Investigations of full phase-space structures include accurate simulations of two dimensional phase-space (Alard & Colombi 2005; Colombi & Touma 2007) and analyses relying on a metric approach to six dimensional phase-space in N-body simulations (Vogelsberger et al. 2008; White & Vogelsberger 2008).

A particularly important step in understanding dark matter clustering lies in an analysis of the bound structures found in N-body simulations. This is at present usually carried out with structure finders such as SUBFIND (Springel et al. 2001), ADAPTAHOP (Aubert, Pichon & Colombi 2004) or PSB (Kim & Park 2006). Following this path, we present a new multi-dimensional Hierarchical Structure Finder which complements all the above numerical methods with an effective and robust analysis of phase-space structures in full 6D space.

The paper is organised as follows. First, we review current structure finders in Section 2. We then present our new multi-dimensional Hierarchical Structure Finder (HSF) in Section 3. In Section 4, we use our algorithm to detect and analyse phase-space structures of a large halo taken from the Millennium Simulation. We investigate the space of parameters on which our HSF algorithm depends and try to find the best choice of the parameters according to the application under consideration. We also introduce the simulation merger tree to follow the evolution of structures in phase-space. This allows us to analyse in detail a few representative cases. This is followed by a quantitative analysis of HSF structures in the space and time domain. We also discuss the bimodal nature of the substructure population, in terms of bound structures versus tidal tails and tidal streams. Finally, in Section 5 we give a summary and present our conclusions.

2   STRUCTURE FINDERS

An important step in the analysis of cosmological N-body simulations is to search for virialized dark matter haloes. These are commonly defined as regions around local density maxima enclosed by a certain isodensity contour. The exact definition of such a border changes from method to method. The simplest and the most popular technique for finding virialized haloes is the friends-of-friends (FOF) method (Davis et al. 1985), which links together particles which are separated by less than a fixed length b. Usually b is set to 0.2 times the mean inter-particle separation, which corresponds to finding haloes with overdensity approximately equal to 178 times the mean background density ρ_{mean} (Cole & Lacey 1996). The mass function of haloes identified by the FOF method is in good but not perfect agreement with the predictions of the Press-Schechter theory. However, the method tends to link together structures across fine bridges (e.g. Lukić et al. 2008) and it is not capable of detecting substructures inside the virialized haloes themselves. A comparable method is the spherical overdensity algorithm (SO, Lacey & Cole 1994) which searches for local density peaks and then grows around them spheres out to a radius where the enclosed mean density satisfies a prescribed overdensity criterion. By definition, the SO method finds only spherical structures. It does not link structures together with artificial bridges as FOF does, but it may count mass twice in certain cases.

However, for current high resolution simulations, one needs to find not only isolated haloes but also their internal substructures. One of the first methods which made it possible to find such structures is the hierarchical friends-of-friends scheme (Klypin et al. 1999), in which a set of different linking parameters, b, is used to identify multiple levels of substructures inside haloes.

To distinguish haloes and their substructures in rich environments, each detected structure is then usually tested against an additional binding criterion. This dynamical criterion uses information from velocity space to guarantee that each structure not only exists but will survive for a longer period of time.

In the spirit of the SO and FOF methods, the bound density maxima (BDM, Klypin et al. 1999) and DENMAX (Gelb & Bertschinger 1994) methods were proposed. In BDM, particles are grouped in spheres around local density maxima and are then progressively unbound. In DENMAX, particles are grouped together when they converge to the same local density maximum if they are moved along local gradients, calculated on a rectangular grid. In a final additional step they are attached to groups identified by the FOF method and then their total binding energy is checked. This method was generalised in the SKID algorithm (Governato et al. 1997), in which the local density and its gradient are calculated directly at the particles positions with the SPH method. A similar but simpler method was implemented in the HOP algorithm (Eisenstein & Hut 1998), in which each particle is connected to the one with the highest density (found by SPH) among its N_{ngb} closest neighbours (with N_{ngb} ranging typically between 10 and 20). In this way, space is divided into peak-patches that are then combined into the final structures.

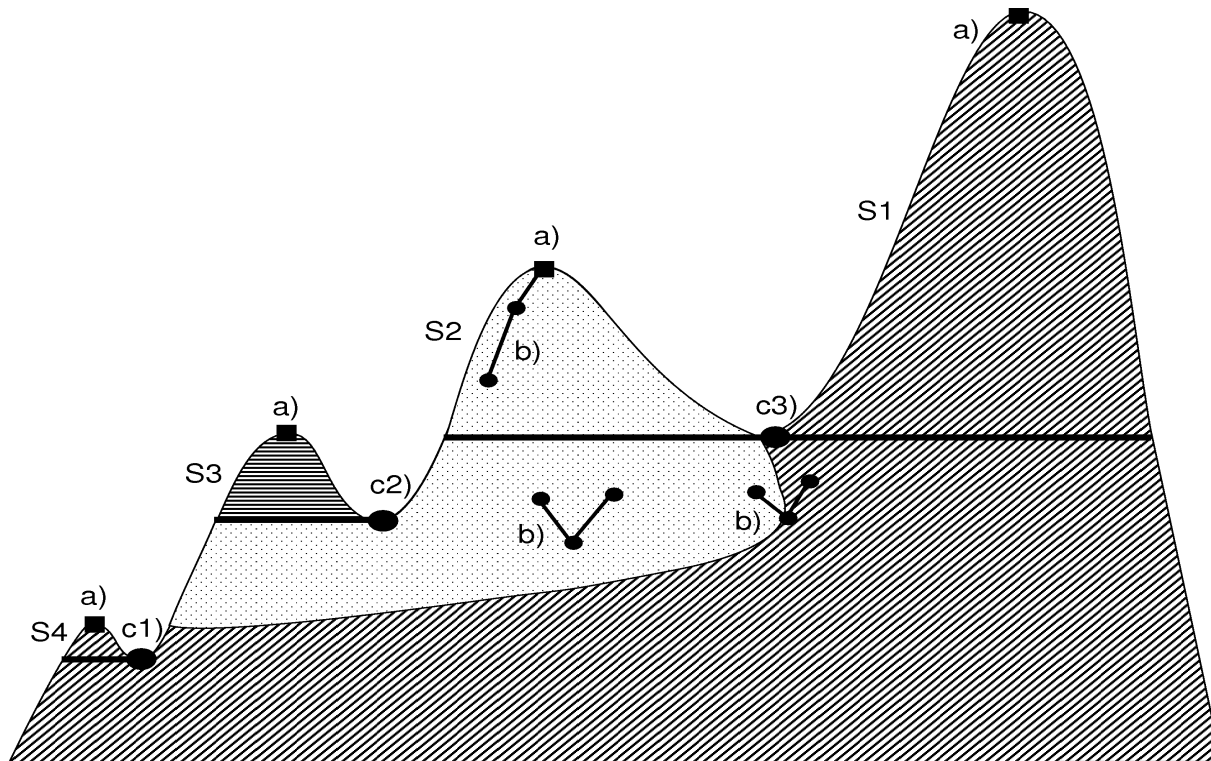The HOP method gave rise to new structure finders

Figure 1. Sketch of the hierarchical structure finder. S1, S2, S3 and S4 are four different structures found by the HSF algorithm. We start to grow structures from local maxima which are marked with (a). We grow them down by looking at local neighbours with higher density (b), and we connect particles properly to structures. Particles on the border of two structures are always connected to the larger one. When we find a saddle point (c) we first apply our Poisson noise criterion. When the structure is not significant (S4), we connect all its particles to the most massive partner (c1). If both structures are significant, we apply to them the cut or grow criterion, and when one structure is significantly less massive than its companion, we grow only the most massive one (c2), or if structures have comparable masses, we grow both of them (c3).

such as SUBFIND, ADAPTAHOP, VOBOZ and PSB. The differences between them are sometimes quite subtle. In SUBFIND (Springel et al. 2001), each particle marks its two closest neighbours with higher density among the N_{ngb} closest ones. Then particles are sorted by SPH-density in descending order. Particles without higher density neighbour are marked as the centres of new structures (local density maxima). Then the structures grow down in density till they reach border particles, called saddle points, which have two higher density neighbours belonging to two different structures. The smallest structure is marked as a structure candidate and then both structures are joined together. Structure candidates are arranged in a hierarchical tree and are successively unbound, going from bottom of the tree to the top. Particles which are not bound to a structure are attached to its larger parent structure.

Even though ADAPTAHOP (Aubert, Pichon & Colombi 2004) constructs the tree of structures in the opposite way to SUBFIND, from bottom to top, the main ideas are very similar. First, it grows peak-patches around local density maxima as in HOP and then finds border particles and saddle points among them. In addition to SUBFIND, each structure is checked against Poisson noise to infer its level of significance. In ADAPTAHOP, contrary to SUBFIND, only particles above saddle points define structures. VOBOZ (Neyrinck et al. 2005) on the other hand uses Delaunay tessellation to define

particle densities and neighbourhood relations, and also checks the significance level of structures against a specific Poisson noise criterion. The PSB algorithm (Kim & Park 2006) uses a grid as in DENMAX to find local density maxima and saddle points, but then constructs a hierarchical structure tree in the same way as in SUBFIND. In PSB, particles below saddle points are first attached to all structures which are above them and then are assigned to individual structures following the process of unbinding. In addition to the standard unbinding procedure, PSB takes into account tidal force criteria.

Even though many of the above structure finders use velocity information for the purpose of a gravitational unbinding procedure, none of them uses the full six dimensional phase-space information. However, the advantage of such an approach is that structures can be defined in a much more natural way in phase-space. In particular, they have a higher contrast than in position space. In fact, many structures such as streams and caustics are well defined only in phase-space. 6D FOF (Diemand et al. 2006) is the first implementation of a structure finder working directly in phase-space. It is conceptually a simple extension of FOF based on a six dimensional distance measure, using a fixed global scaling between position and velocity space. The proposed method finds only local phase-space density maxima and then grows spheres around them like in BDM algorithm.

In this paper, we propose a new universal multi-

dimensional Hierarchical Structure Finder (HSF) which is used here to find phase-space structures in cosmological N-body simulations. The algorithm employs, in a higher number of dimensions, a similar approach to SUBFIND and ADAPTAHOP, but with a new and very effective cut or grow criterion, controlled by a *connectivity parameter* α, to separate accurately structures from each other.

3 THE HIERARCHICAL STRUCTURE FINDER (HSF)

Our goal is to find the hierarchy of dark matter haloes and subhaloes, which are defined by locally overdense regions in phase-space. The main difference between our approach and previous structure finders is that we focus on all kind of phase-space structures even those which are not self-bound, such as tidal streams. To enable comparisons, we however implement, in addition to our base algorithm, also an unbinding step. The HSF can be run on a full simulation to detect all the haloes and the subhaloes population, or on standard groups found by a FOF algorithm with, e.g., $b = 0.2$.

Prior to the identification of structures, our HSF algorithm estimates the local phase-space density and the local phase-space neighbourhood of each particle in the sample. Following the proposal of Maciejewski et al. (2008) for optimum local phase-space density estimation, we use the SPH method with N_{sph} neighbours found in the adaptive metric computed by the EnBiD algorithm[1] of Sharma and Steinmetz (2005). We performed a small modification of the EnBiD algorithm to make possible the output for each particle of the phase-space neighbourhood with N_{ngb} closest neighbours among the N_{sph} (in the proper local adaptive metric frame). It is worth mentioning that both phase-space density and neighbourhood estimations by the EnBiD algorithm are computationally inexpensive and are almost as fast as standard three-dimensional SPH estimators.

We define *phase-space structures* as the regions grown around local density maxima by following the local density gradient. To find such structures, HSF uses a modified version of SUBFIND, which redistributes particles below saddle points in a new fashion. In the first step, the HSF algorithm finds locally overdense regions in phase-space by tracing isodensity contours identified by saddle points. In addition, we test on each saddle point if structures are statistically significant when compared to Poisson noise as in ADAPTAHOP. Particles below phase-space isodensity contours can in principle be attached to many structures simultaneously but our aim is to attach each of them to only one structure. To do that, we use a simple but robust cut or grow criterion depending on a *connectivity parameter* α, which allows us to reconstruct a multilevel hierarchy of structures within structures. In our implementation, each saddle point defines a connecting bridge between two structures. Particles below this saddle point are attached to one of the structures, or are redistributed between both of them according to the structure masses. We here consider two different cases:

• the two structures have comparable masses: we attach

particles below the isodensity contour to both structures in the same manner as above the isocontour. Border particles are attached to the most massive structure;

• one structure is significantly less massive than the other one: we mark it as a structure and attach all particles below it only to the most massive one.

While we apply the cut or grow criterion, we create a hierarchical binary tree of structures by connecting each structure to its more massive partner if one exists. This way of cutting works like a second Poisson noise criterion and it allows one to grow only structures which are significant.

In detail, the HSF algorithm, sketched in Figure 1, works as follows:

(i) For each particle, we estimate the local phase-space density with SPH-AM and the local adaptive metric environment using N_{ngb} neighbours. We usually perform the SPH interpolation with $N_{sph} = 64$. This value represents a good compromise between filtering of Poisson noise and identification of faintest significant structures. We find that the final results are rather insensitive to the choice of N_{ngb}. Our favourite value is $N_{ngb} = 20$, similar to what is used with HOP, ADAPTAHOP and SUBFIND. Then for each particle, we find the set A of its neighbours among the N_{ngb} which have higher density than the particle. We sort the set A ascendingly according to local neighbourhood distances (closest particles are in the beginning of the list). Then we take the two closest elements of A and put them in a second set B. This set can be empty or contain one or two elements.

(ii) We sort the particles by decreasing phase-space density and, following this ordering, we attach each particle to different structures according to the following rules:

(a) The set B is empty. This means that the particle does not have any neighbour with higher density: we found a local maximum and we mark the particle as the beginning of a new structure.

(b) The set B contains one or two particles which belong to the same structure: we attach the particle to this structure; or set B contains two particles which belong to different structures S_m and S_n, and the S_m structure is marked as a more massive partner of S_n: particle is attached to S_m (this is a border particle).

(c) The set B contains two particles which belong to different structures S_m and S_n and the structures are not on each other's more massive partner list: it means that we found a saddle point and we perform the marking $S_m > S_n$, $S_n > S_m$, or $S_m \simeq S_n$.

The way this marking is performed in detail can be described as follows:

(1) First, we check the level of significance of structures S_m and S_n when compared to Poisson noise (Aubert, Pichon & Colombi 2004). Let $\langle S_m \rangle$ and $\langle S_n \rangle$ be the first and the second structure's average density and ρ_{saddle} be the density of the saddle point connecting them. Each structure is significant if

$$\langle S \rangle > \rho_{saddle} \left[1 + \frac{\beta}{\sqrt{N}} \right], \tag{1}$$

where β is the "$\beta\sigma$" level of significance of the structure (in our tests β is set between 0 and 4), and N is the number of particles belonging to the structure. If one

---

[1] SPH-AM in the notation of Maciejewski et al. (2008)

of the structures is not significant, then we attach all of its particles to the second structure. In the case where both structures are not significant, we attach all the particles to the structure which has the highest maximum density.

(2) If both structures are significant compared to Poisson noise, we test them against the cut or grow criterion. Let $|S_m|$ and $|S_n|$ be the masses of our structures up to this saddle point and $|S_m| > |S_n|$, then we mark structure S_m as more massive partner of S_n. If $|S_m|\alpha > |S_n|$, with $\alpha \in]0,1]$, then structure S_n is more than $1/\alpha$ times less massive than S_m and we attach all the particles below this saddle point to S_m.

(3) If $\frac{|S_m|}{|S_n|} \in]\alpha, \frac{1}{\alpha}[$, we consider that both structures have the same order of mass: we attach the saddle point to the most massive structure and all particles below are attached according to the rules we set before.

(iii) Finally, a structure containing less than N_{cut} particles is considered insignificant, and all its particles are attached to its more massive partner. If a structure with less than N_{cut} particles does not have a more massive partner, we put it on the list of *fuzzy* particles.

(iv) At the end of this process, we obtain a hierarchical tree of structures. Each particle belongs only to one structure or to the background (fuzzy list). In addition, we add to our algorithm a final step in which we check each structure against an unbinding criterion. Once we have marked its more massive partner for each structure, we sort them recursively such that the larger partners (parents) are always after the smaller ones (children). Then we unbind structure after structure from children to parents and add unbound particles to the larger partner. For each individual structure, we calculate the gravitational potential. We set the structure centre as the position of the particle with the minimum potential and the velocity centre as the mean velocity. We calculate the kinetic energy of each particle relative to the mean velocity of the structure. All the particles with positive total energy are marked and, in that ensemble, 1/4 of the ones with positive total energy are removed. We repeat this process iteratively (starting with a new gravitational potential calculation) up to the moment when we stay with bound particles only. If the structure has less than N_{cut} particles after the unbinding process, then we mark it as not bound and attach all its particles to its more massive partner or put them on the fuzzy particles list. To speed up the calculation of the gravitational potential, we use the tree algorithm implemented in GADGET-2 (Springel 2005).

Most halo finders such as DENMAX, BDM, SKID, SUBFIND, ADAPTAHOP and VOBOZ use a two step procedure for finding the structures. First, they assign as many particles as possible to each individual structure in three dimensional space by tracing local overdensities (Figure 2, top left panel). When we move to phase-space diagram (Figure 2, top right panel), we however immediately observe that there are many particles belonging to different velocity structures. The unbinding process (Figure 2, second row of panels) then cleans up all these spurious velocity structures. In the four bottom panels, one can observe the results obtained with the six dimensional HSF algorithm. This method allows us to attach particles to structures in a more natu-
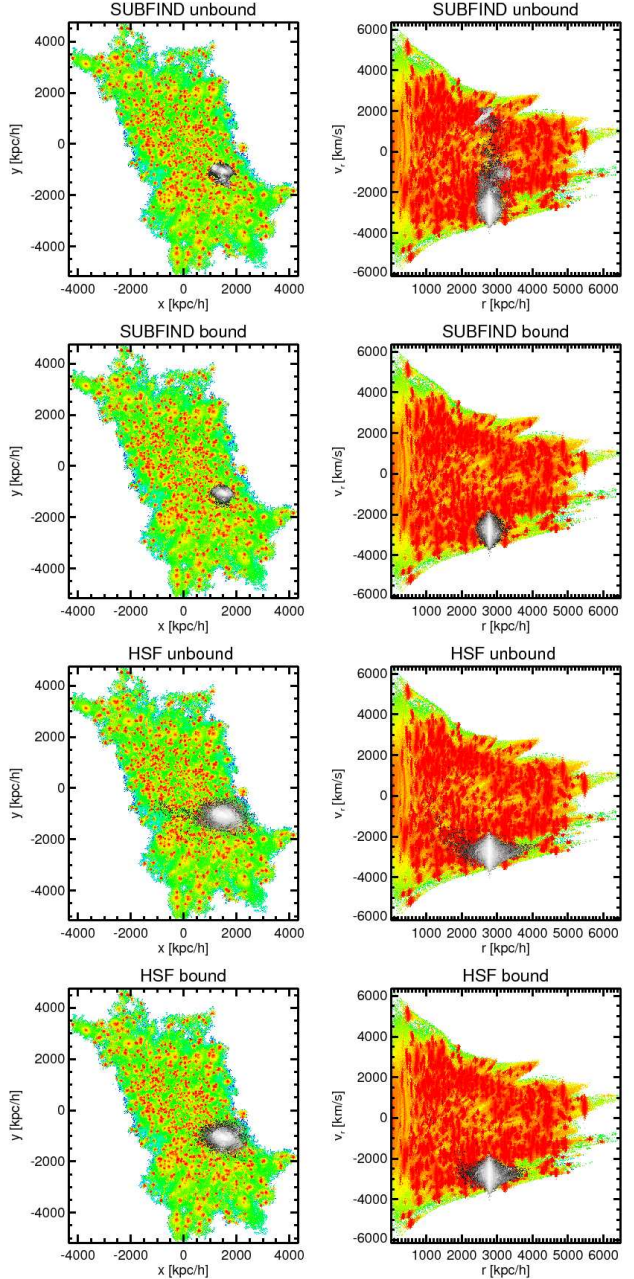

Figure 2. Appearance of our Millennium simulation halo (colour ranging from green to red, scaling logarithmically with phase-space density) and superposed to it, one of its largest substructures found by different algorithms (grey pattern). *Left panels: x-y* position space; *right panels:* radius r - radial velocity v_r phase-space. From top to bottom, the grey pattern corresponds to the substructure found respectively by (i) SUBFIND before unbinding, (ii) SUBFIND after unbinding, (iii) HSF before unbinding, (iv) HSF after unbinding.

ral way, because it treats both position and velocity space (Figure 2, third row of panels). Note that, after unbinding, the structures detected by the HSF algorithm are more extended than with standard algorithms working in position space (Figure 2, bottom panels), an indication that more of the mass belonging to the substructures is recovered.
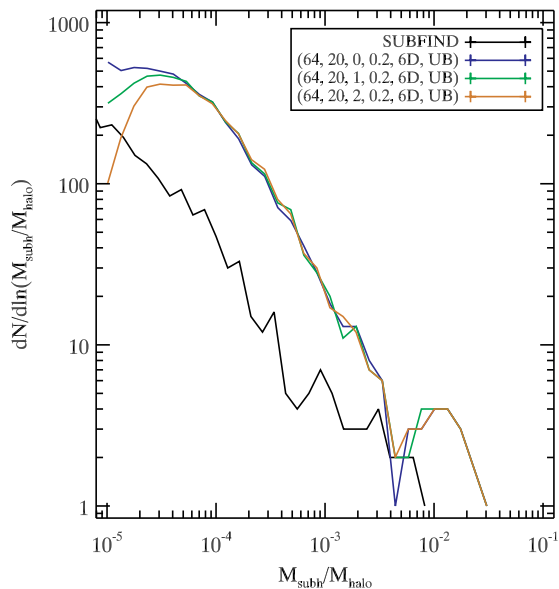
Figure 3. Mass distribution of the substructures as a function of the ratio between the substructure mass and the mass of the main halo. Here, the influence of the choice of the shot noise control parameter β (Eq. 1) on the mass profile is tested.

Figure 4. Mass distribution of the substructures as a function of the ratio between the substructure mass and the mass of the main halo. Here, the influence of the connectivity parameter α and the importance of the unbinding process are tested.

4   RESULTS FOR A TEST HALO FROM THE MILLENNIUM SIMULATION

To test our algorithm we use a large halo extracted from the Millennium Simulation (Springel et al. 2005a). The main cosmological parameters of this ΛCDM-simulation are: $\Omega_m = 0.25$, $h = 0.73$, $\Omega_\Lambda = 0.75$ and $\sigma_8 = 0.9$ ($H_0 = 100h$ km s^{-1} Mpc^{-1}). The simulation volume is a periodic box of size $500\,h^{-1}$Mpc and individual particles have a mass $8.6 \times 10^8\,h^{-1}$M$_\odot$. In our analysis we take the second largest FOF halo at redshift $z = 0$, which has 3.83×10^6 particles.

This section is organised as follows. In Section 4.1, we discuss the influence of the main parameters in our algorithm on the results. In Section 4.2 we use the merger tree history to follow both qualitatively and quantitatively the evolution of structures. In particular, the structures identified by HSF are cross-correlated with their counterpart prior to merging with the main halo. Finally Section 4.3 studies the properties of the substructure population obtained with HSF and its bimodality in terms of bound structures versus unbound tidal tails and tidal streams.

4.1   Choice of the main parameters in the algorithm

In the following, we check the influence of the different parameters on the structures found by our HSF algorithm. A basic parameter setup is given by $N_{\rm sph} = 64$, $N_{\rm ngb} = 20$, $\beta = 0$, $\alpha = 0.2$, $N_{\rm cut} = 20$. We adopt the notation $(N_{\rm sph}, N_{\rm ngb}, \beta, \alpha, {\rm dimension}, {\rm (B)ound/(UN)bound})$ to label each set of parameters. When the dimension is set to 3D, we mean the three dimensional position space, whereas 6D means six dimensional phase-space. Unless mentioned otherwise, we use the HSF algorithm without additional un-
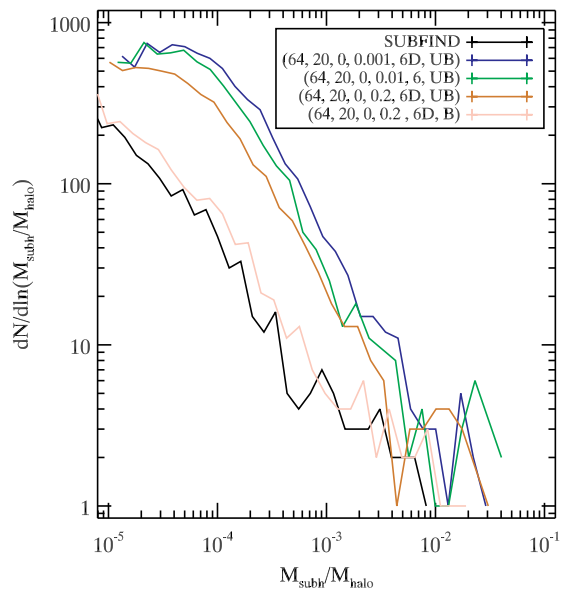
binding step. SUBFIND is in fact one of the versions of our algorithm, characterised by the following parameter setup $(64, 20, 0, {\rm always~cut~smaller~partner}, {\rm 3D}, {\rm B})$. In our analysis, we shall call all the particles in a FOF group *a halo*, the largest structure of the FOF group *a main halo*, and all other structures *substructures*.

Figures 3 and 4 present the number of substructures per logarithmic mass bin scaled to the main halo mass. While testing the different parameter setups, we find that α and β are the most influential. Figure 3 shows that parameter β is important for the smallest structures: visual inspection suggests that a higher β helps to preserve small scale connectivity, e.g. between tidal tails and the bound component of the substructures. The connectivity parameter α has a similar effect, but on the whole mass range instead of small structures only, as illustrated by Figure 4. Because of the partial degeneracy between α and β, we prefer to use $\beta = 0$ in most of our analyses. The choice of α indeed influences connectivity as follows: when $\alpha = 0.2$, the main halo always wins the cut or grow criterion and all structures are cut by it; when $\alpha = 0.02$, the largest substructures can grow inside the main halo; when $\alpha = 0.01$, all small substructures grow more aggressively and the halo is divided into more small parts. In brief, focusing on bound structures calls for a value of α of the order of 0.2, while if one is interested in all substructures including tidal streams, it is better to set $\alpha \simeq 0.01 - 0.02$. In the later case, tuning up β can help to control the small scale connectivity.

Using our base parameter setup, we now compare HSF bound structures with those given by SUBFIND. The HSF algorithm works in six dimensional phase-space, where the distribution of particles shows much more contrast than in position space alone. Because of that, HSF can better trace contours of individual substructures and attach more parti-
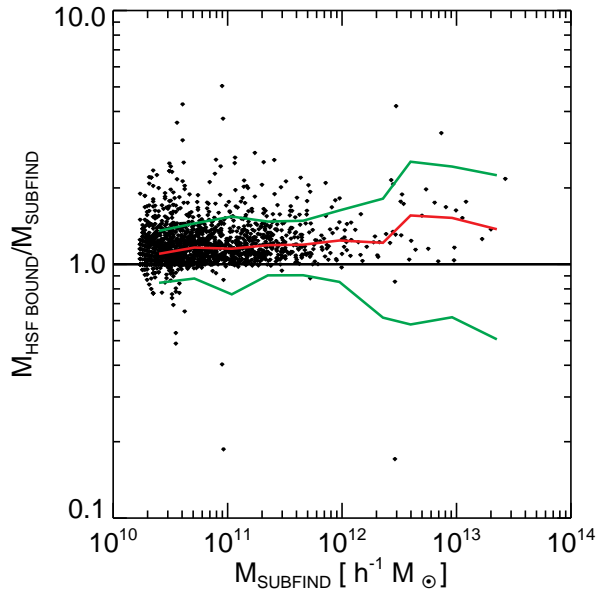
identify the same set of more massive structures, confirming the results above.

4.2 Phase-space structures and merger tree

In the following sections we describe a method to follow back in time the structures detected by our HSF, paying particular attention to the definition of what we use for initial halo. Then we study in detail a set of specific but representative cases. The goal of this analysis is to physically understand the nature of the structures found by our algorithm, before and after unbinding. In particular, we aim to separate clearly tidal streams from compact bounded subhaloes. With the additional time information, we can also associate tidal streams to objects in the stage they were prior to merging with the main halo. We can also study quantitatively how in general phase-space structures evolve in time.

4.2.1 Evolution with time and the merger tree

To study in detail the nature of phase-space structures found by the HSF algorithm we use the merger tree history[2] to follow their evolution backwards in time. Then we count how many particles are shared between each structure prior to merging with the main halo and its counterpart detected by HSF at $z = 0$. This process uses pieces of information which are already available for the processed Millennium Simulation (Springel et al. 2005b) and it is divided into three steps: (i) crosscorrelating the HSF structure catalogue with the SUBFIND one, (ii) following the evolution of SUBFIND structures using the already implemented merger tree history and (iii) using each particle's universal index[3] to follow structures at different output times. We now explain each of these steps in turn.

(i) cross-correlation between HSF and SUBFIND: Information about structures in the Millennium Simulation is organised in terms of two levels: first, particles are attached to different FOF groups (found with $b = 0.2$). Then, in each FOF group, they are separated into the main halo, the substructures found by SUBFIND, and unbound 'fuzzy' particles if present. Running the HSF algorithm with the base parameter setup (64, 20, 0, 0.2, 6D UB/B) provides a phase-space structure list. Then, for each member of that list, the SUBFIND substructure sharing the largest possible number of particles with it is identified. If the HSF structure shares less than 20 particles with any SUBFIND substructure, it is put into an unmatched list. In the opposite case, we call this SUBFIND substructure a *seed* of the HSF structure.

Figure 5. Ratio of mass of each HSF bound structure divided by the mass of its SUBFIND counterpart as a function of SUBFIND structure mass. The central curve corresponds to the median value of the ratio calculated over 10 logarithmic bins along the x-axis, taking into account only bins containing 2 points or more. The two additional green curves on each side show $1\,\sigma$ errors estimated from the variance of points in each bin.

cles to them. Even after the unbinding step, HSF therefore attaches more particles to the substructures than SUBFIND. This is illustrated by Figure 5, where the ratio between the mass of HSF bound structures and the mass of their SUBFIND counterparts is plotted: HSF attaches on average ~ 1.1 more mass to small structures than SUBFIND and up to twice more to the largest ones.

The left panels of Figure 6 compare bound structures found by both methods in position space. The area of each circle is proportional to the structure mass.

With the parameters set up chosen here, HSF finds around 10% more structures, mostly small ones, in the outskirts of the main halo and clearly attaches more mass than SUBFIND to most of them. Nevertheless, the spatial distributions of HSF and SUBFIND substructures are nearly the same, as expected. To complete this visual inspection, the right panels of Figure 6 compare the 200 largest bound structures found by both methods. Most of the HSF structures are matched by SUBFIND, except that they are more extended. As mentioned before, many of these structures have $1.1 - 2$ times more mass in HSF than in SUBFIND. Interestingly, this confirms the mass excess found around SUBFIND substructures in a comparison of simulation with gravitational lensing observations by Natarajan, De Lucia & Springel (2007).

If bound substructures are counted as a function of maximum circular velocity instead of mass, a much closer agreement is found, however. This is seen in Figure 7, where the cumulative velocity functions of bound substructures for HSF and SUBFIND are compared. HSF tends to find a few more small substructures, but both algorithms essentially

---

[2] Each branch of this tree corresponds to the evolution in time of a dark matter halo as a stand alone structure, while each node of it corresponds to the event of merging between 2 halos or more. Note that, due to the collisionless nature of dark matter, the halos can pass through each other and separate again: in practice, the structure of such a tree can be non-trivial.

[3] The universal index of a particle is just a number associated to each single particle in order to identify it unambiguously, which is useful for analyses of Lagrangian nature such as performed in this work.
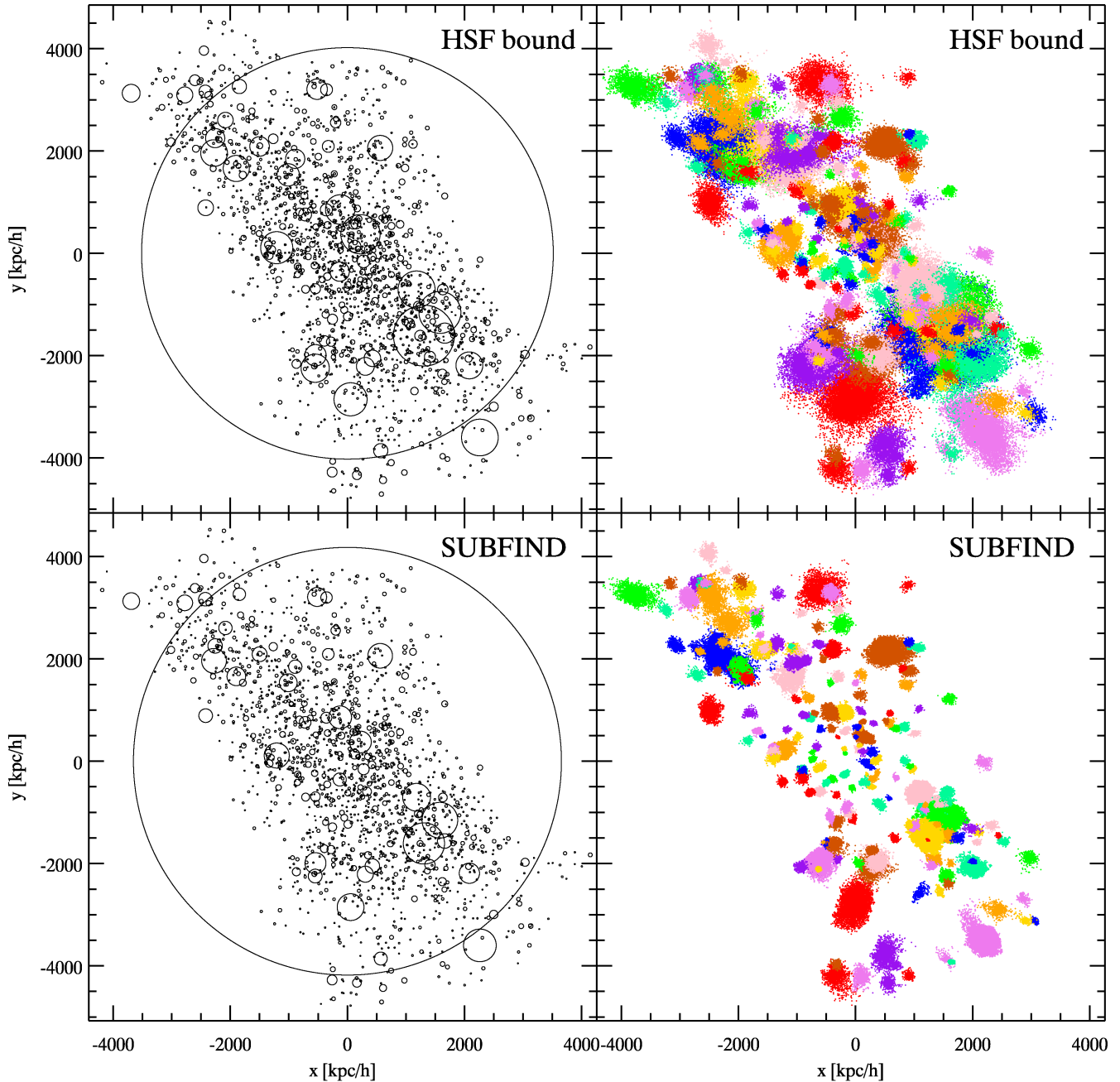
Figure 6. *Left side panels*: Spatial distribution of HSF bound structures and SUBFIND structures, with at least 20 particles. The area of each circle is proportional to the structure mass. *Right side panels*: First 200 most massive bound substructures identified by HSF and their SUBFIND counterparts. Particles belonging to the same substructure share the same colour.

(ii) Following SUBFIND structures back in time: Information about the time evolution of structures is stored in the Millennium Simulation in a merger tree (more details in Springel et al. 2005b). We use the tree information which gives for each halo or substructure its most massive progenitor, if there is any. Once the list of seed SUBFIND substructures is obtained, each of them is traced back in time by following its most massive progenitor recursively up to the moment when this past structure was the main halo of a FOF group. This is the last occurrence of the struc-

ture as being distinguishable as an isolated halo. We store the redshift of this event and all particles belonging to the main halo found in this way are denoted as the *initial halo*. There is a small number of substructures which do not have a proper progenitor, they are dropped from the analysis.

(iii) Using each particle's universal index to follow structures at different times: In the last part of the procedure, we link together the information gathered in the previous two steps. For each HSF structure identified at the present time, we find its initial halo and, with the help of universal
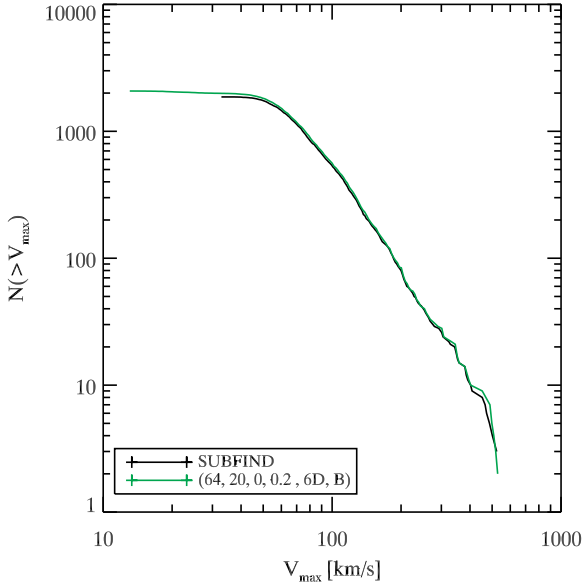
Figure 7. Cumulative count of substructures as a function of maximum circular velocity. We here compare results of HSF for bound structures with substructures identified by SUBFIND in the same halo.

indices, we identify *shared* particles, i.e. particles belonging both to the initial and final structures. We carry out exactly the same analysis for HSF bound structures and for SUBFIND itself.

In addition, during this process, we gather for each substructure information about the position of its centre and its velocity at various times (we use the SUBFIND definition for the structure centre), and similarly for the position and velocity of the centre of the main halo. With these pieces of information at hand, we can define an orbital count by determining the number of times a substructure's radial velocity with respect to the centre of the halo changes sign, which each time signals completion of what we call an orbit. This definition requires that there are enough snapshots to catch orbit details. This is the case for most substructures, probably all, although this statement is not easy to check rigorously.

4.2.2 Definition of the initial halo

In our analysis of the time evolution of the structures, we adopt the main haloes of the FOF groups found by SUBFIND as 'initial haloes'. Another possibility is to chose for each initial halo all the particles belonging to the FOF group. In the first case, the analysis is simplified by the fact that we look only for the evolution of one isolated component. However this component represents only one part of the halo. In the second case, a FOF group can sometimes have a few main halo candidates joined by small artificial bridges (up to 20% of FOF groups show such a feature, e.g. Kim & Park 2006) but can in fact be tidally disrupted such that its components get away from each other.

To demonstrate the effects described above, we choose

one particular structure in our test halo. The top panel of Figure 8 shows all the particles belonging to the initial halo traced to redshift $z = 0$, while the second row of panels corresponds to the full traced initial FOF group. This structure goes around the main halo one time (its orbit is shown in the third row of panels of Figure 9). The initial FOF group is tidally disrupted during this process and its various components are clearly separated from each other. SUBFIND recognises the central part of the bound object (bottom panels of Figure 8). The HSF bound structure contains more particles (fourth row of panels in Figure 8). These particles belong to tidal tails, but are in fact still gravitationally linked to the structure. The HSF structure (prior to unbinding) contains 55% of the particles of the initial halo, and reproduces perfectly its shape (on third row of Figure 8).

4.2.3 Qualitative analysis of structure evolution

To better understand all the processes at play during structure evolution, we study in greater detail eight different cases displayed in Figure 9. The colours in the figure are coded as follows:
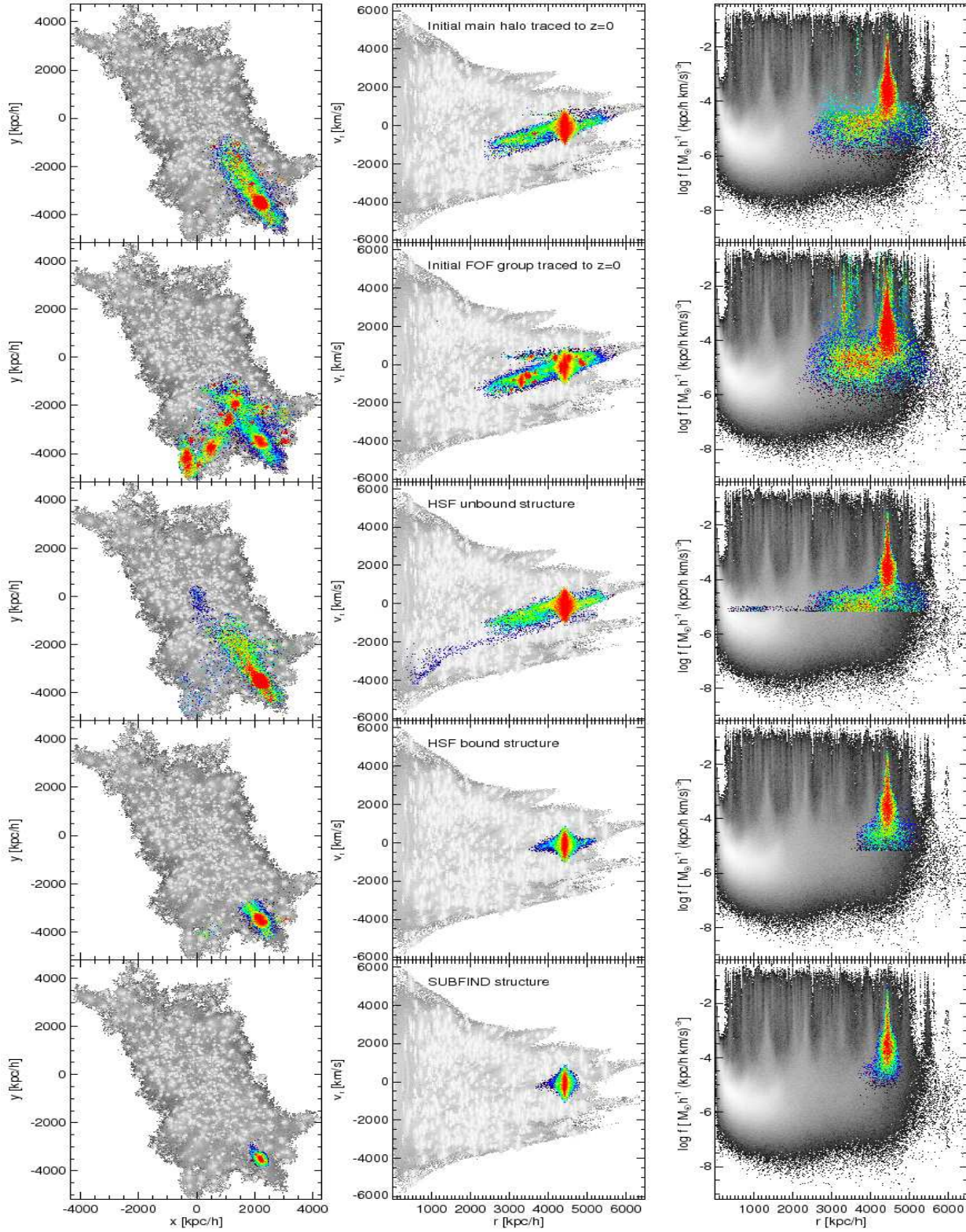
• Green and red particles belong to one structure found by the HSF algorithm (without unbinding): green particles belong to the initial halo, while the red particles do not belong to it.
• Black particles belong to the SUBFIND seed of the HSF structure.
• Blue particles belong to the initial halo, but do not belong to the HSF structure.
• Yellow particles belong to the initial halo and belong to any HSF structure, besides the one we take for the current analysis. We mark particles in yellow only for structures in the last three rows of panels of Figure 9.

The particles are plotted in the following order: blue, red, green, black, and finally yellow. Various structures parameters are listed in Table 1, for each of the 8 cases considered here. The pink curve shows the orbit of the object inside the main halo. We now discuss in detail each of these 8 cases.

(i) The first case corresponds to the largest structure found by HSF. It entered the main halo recently, at redshift $z = 0.17$. HSF identifies a large fraction of 84% of the initial structure, and unbinding worsens that number by only about 3%. On the other hand, SUBFIND identifies only 37% of the content of this rather massive structure.

(ii) The second structure is at a moment just before crossing for the first time the main halo centre and starts to be significantly tidally disrupted. The HSF structure still contains 97% of particles of the initial main halo, while the SUBFIND bound structure accounts for only 26%. Indeed, HSF manages to attach to the structure unbound particles which already crossed the main halo centre and contribute to a tidal tail.

(iii) The third structure entered the halo at redshift $z = 0.56$ and made an orbit inside it. This is the reason why we identify only 55% of the initial structure, but still more than SUBFIND (35%). HSF attaches some additional particles to the structure, i.e. particles that do not belong to the initial main halo, but in fact we found that a large fraction of them belong to the initial FOF group.
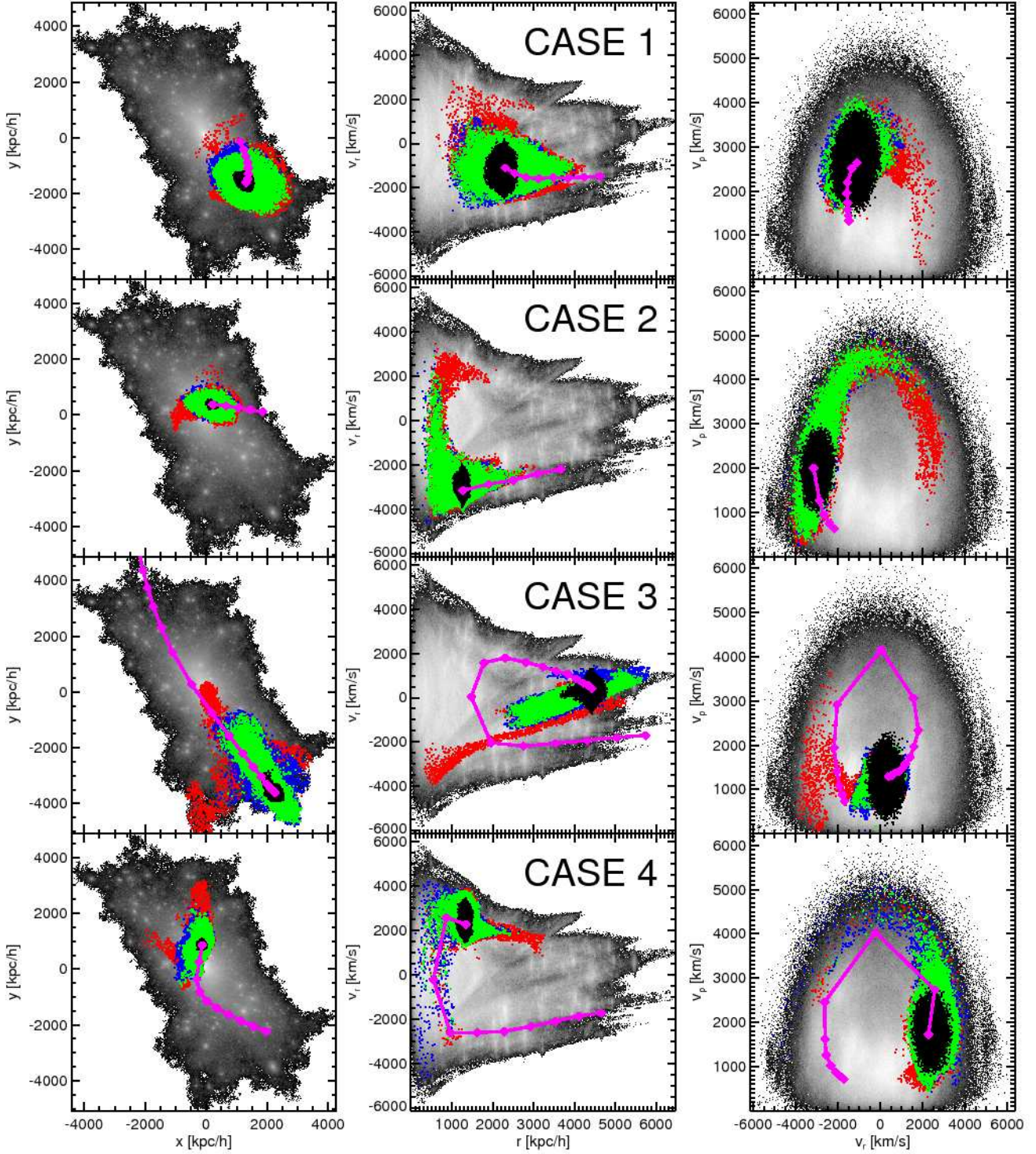
Figure 8. Follow up of a particular substructure (in colour) of our Millennium test halo (in grey). *From left to right: x–y* position space, radius *r*–radial velocity v_r, radius *r*-phase-space density *f*. In the two left columns of panels, the colour traces the logarithm of the phase-space density (from dark grey to light grey or from dark blue to red). In the right column of panels, the colour just traces the projected particle density. *From top to bottom:* Initial main halo traced to $z = 0$, initial FOF group traced to $z = 0$, HSF unbound structure, HSF bound structure, and SUBFIND structure.

Figure 9. Properties of some chosen structures. From left to right: x–y position space diagram, radius r–radial velocity v_r diagram, radial velocity v_r–tangential velocity v_t diagram. Further description in the text (section 4.2.3).

(iv) The fourth case corresponds to a structure that just passed the main halo centre. 88% of the initial structure is still identified. HSF is capable of connecting to the structure (unbound) particles which were strongly affected by tidal stripping but still belong to the structure. In this case

for example, it joins some particles having high negative velocity.

(v) The fifth case corresponds to the example of a structure that has gone around the main halo centre. HSF identifies 90% of the initial structure and SUBFIND only 44%. We
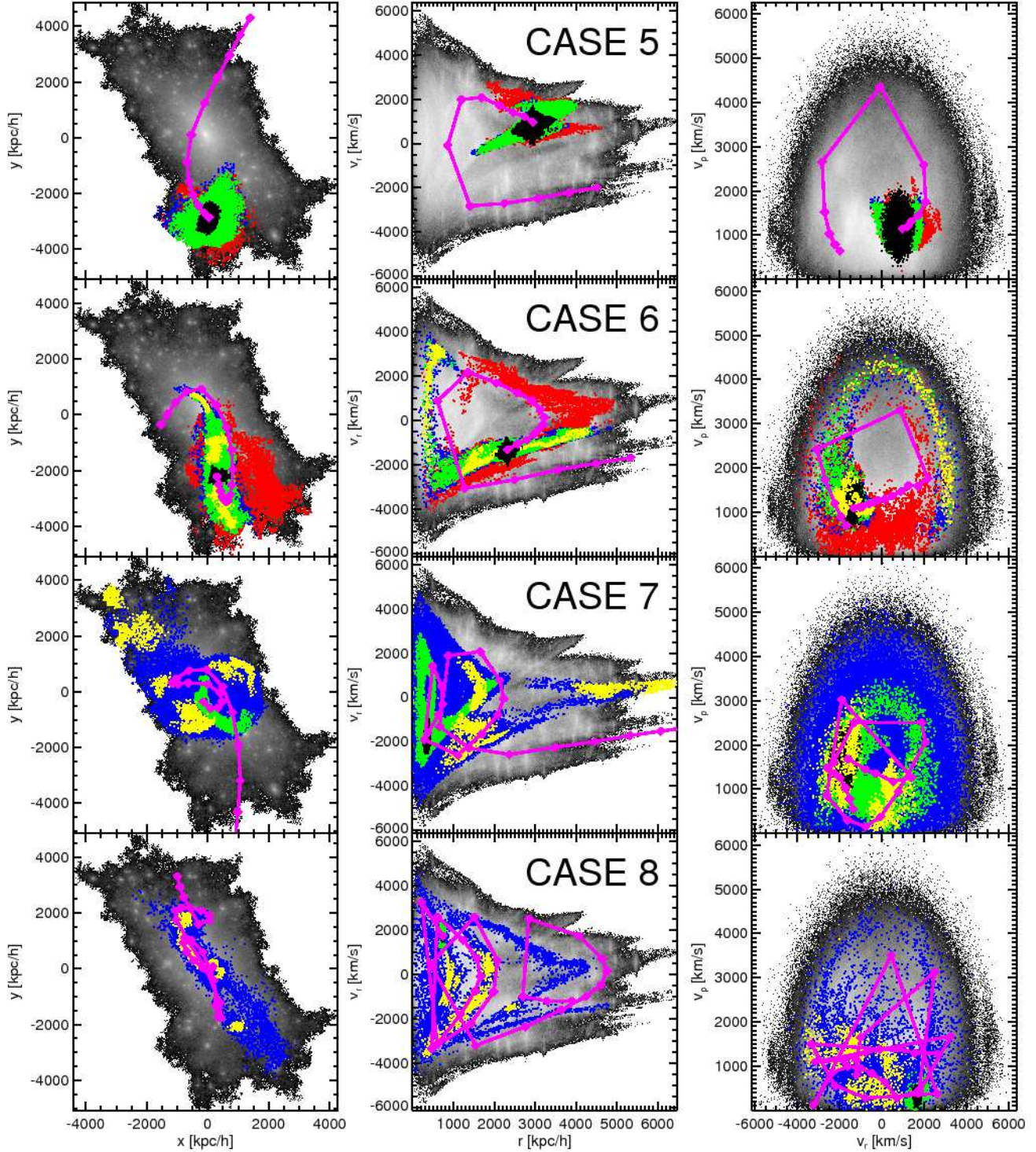
Figure 9. Continued.

can clearly see here the typical "z" shape of the structure in (r, v_r) space, which correspond to a scaled down version of the phase-space diagram of the halo (that we see only in half here).

(vi) The sixth row of panels corresponds to a rare occurrence when HSF partly fails. The HSF structure contains

65% of particles of the initial one. It is falling inside the main halo centre and some of the particles already crossed the centre. Parts of the initial structure are identified as other HSF objects: the initial halo shares 72% of its particles with all detected HSF substructures. There is however a large fraction of particles associated with the HSF structure

Table 1. Properties of eight chosen structures. Column description: *nr.:* structure number, in the same order as listed in the text and in Figure 9; *orbits:* number of orbits inside the main halo; *HSF par.:* number of particles belonging to the HSF structure; *Initial FOF group par.:* number of particles belonging to the initial FOF group; *Initial halo par.:* number of particles belonging to the initial main halo; *SUBFIND:* fraction of the particles of the initial halo that are still identified in SUBFIND (in HSF bound, HSF, any identified HSF structures, respectively for the next columns).

nr.	orbits	z	HSF par.	Initial FOF group par.	Initial halo par.	SUBFIND	HSF bound	HSF	any HSF
1	0	0.17	78791	109835	76567	37%	81%	84%	94%
2	0	0.09	37417	39511	32383	26%	84%	97%	99%
3	1	0.56	36248	85225	53186	35%	44%	55%	57%
4	1	0.24	35520	43202	35463	26%	43%	88%	91%
5	1	0.32	33647	30432	28604	44%	60%	90%	92%
6	1	0.62	17971	17053	14364	32%	38%	65%	72%
7	2	0.83	14477	140799	119621	2%	5%	11%	12%
8	4	1.50	854	10696	9896	3%	6%	8%	25%

(in red) that should just belong to the background. Indeed, we checked that most of them cannot even be associated with the initial FOF group.

(vii) The seventh row of panels shows the typical case of a massive structure which, after only two orbits (so it passed nearby the halo centre only twice), already dissolved in the main halo, because of massive tidal disruption. Even though the HSF structure contains only 11% of the particles of the initial halo, we find that other HSF substructures match some parts of the initial halo: 90% of particles inside such substructures come from the initial halo, although some of them belong to other members of the initial FOF group. In other words, it means that our algorithm is capable of finding remnants of tidal tails. All blue particles can not be distinguished from the main halo anymore and correspond to the part of the structure which has been completely diluted.

(viii) In the last case, we take a structure which merged with the main halo at high redshift $z = 1.5$, and already made four orbits inside. As expected, this structure has experienced strong tidal striping: the HSF structure contains only 8% of the initial structure. Most of it indeed already dissolved inside the main halo. Still, some remnants were identified as disjoint HSF components and represent 25% of the initial structure.

To conclude this section, objects which recently entered the main halo and typically made up to one orbit inside it are in most cases fully recovered by HSF. When the structures make more orbits, they are more tidally disrupted, especially when they come close to the halo centre, so the fraction of particles identified decreases. HSF still finds in most cases remnants of strongly disrupted objects as individual tidal streams detached from the bound component (if this later still exists).

4.2.4 Quantitative analysis of structure evolution

To test the performance of HSF quantitatively, one can for example study the fraction $M_{\mathrm{shared}}/M_{\mathrm{initial}}$ of particles inside the initial halo found at the present time in the corresponding HSF structure, as a function of redshift of merging with the main halo (top left panel of Figure 10) or as a function of initial mass (top right panel of Figure 11). Indeed, one expects a strong correlation between the value of $M_{\mathrm{shared}}/M_{\mathrm{initial}}$ and the initial halo mass and the redshift z

of merging. Obviously, the higher z, the larger the number of orbits (Fig. 12) and the larger the number of particles lost due to tidal stripping (top left panel of Figure 10). At low redshift, $z \lesssim 0.3$, where the number of orbits is typically less than one, there is no strong structure evolution in phase-space and HSF identifies $80 - 100\%$ of the initial structure mass (upper left panel of Fig. 10). There are a few structures at redshift $z \sim 0.1 - 1.0$ for which HSF can find only a very small fraction of their initial mass. All of them are tidal remnants.

The effect of unbinding on the ratio $M_{\mathrm{shared}}/M_{\mathrm{initial}}$ is shown in the lower left panel of Fig. 11 (as a function of mass) and upper right panel of Fig. 10 (as a function of redshift). Obviously, after unbinding, the fraction of particles recovered by HSF decreases significantly, even for a small redshift of merging $z \lesssim 0.3$. Indeed, a significant fraction of the mass in substructures is contained in tidal tails that are very well identified by HSF, at least for $z \lesssim 0.3$, but that are not bound any more to the substructures. Note that, as expected, the SUBFIND (bound) substructures are not very different from the HSF bound ones, except that they contain a slightly smaller fraction of the mass of the initial structures (lower right panel of Fig. 11).

Another important test of our structure finder consists in examining the fraction of particles inside each HSF structure that is shared with the initial halo as a function of initial halo mass (top left panel of Figure 11). HSF finds that for massive objects, $80 - 90\%$ of the present structure mass belongs to the initial halo. For smaller structures, the scatter is higher and only around 40% of the particles found in HSF objects belong to initial halos. This actually means that for many small structures, the HSF algorithm attaches more particles than they had before. This it mainly due to the fact that we consider for the initial stage only the main part of the halo and not its substructures: disentangling substructures from the main halo remains an ambiguous process, and structures identified at the present time can contain part of the mass of the substructures inside the initial halo. In the process, we also do not take into account particles surrounding the initial halo which were not selected by the FOF (yet) but were still infalling onto our Millennium test halo and participate to its background density. As a result, additional particles can be associated to the final HSF structure, and this effect is expected to become stronger if the mass of the identified structure is small.
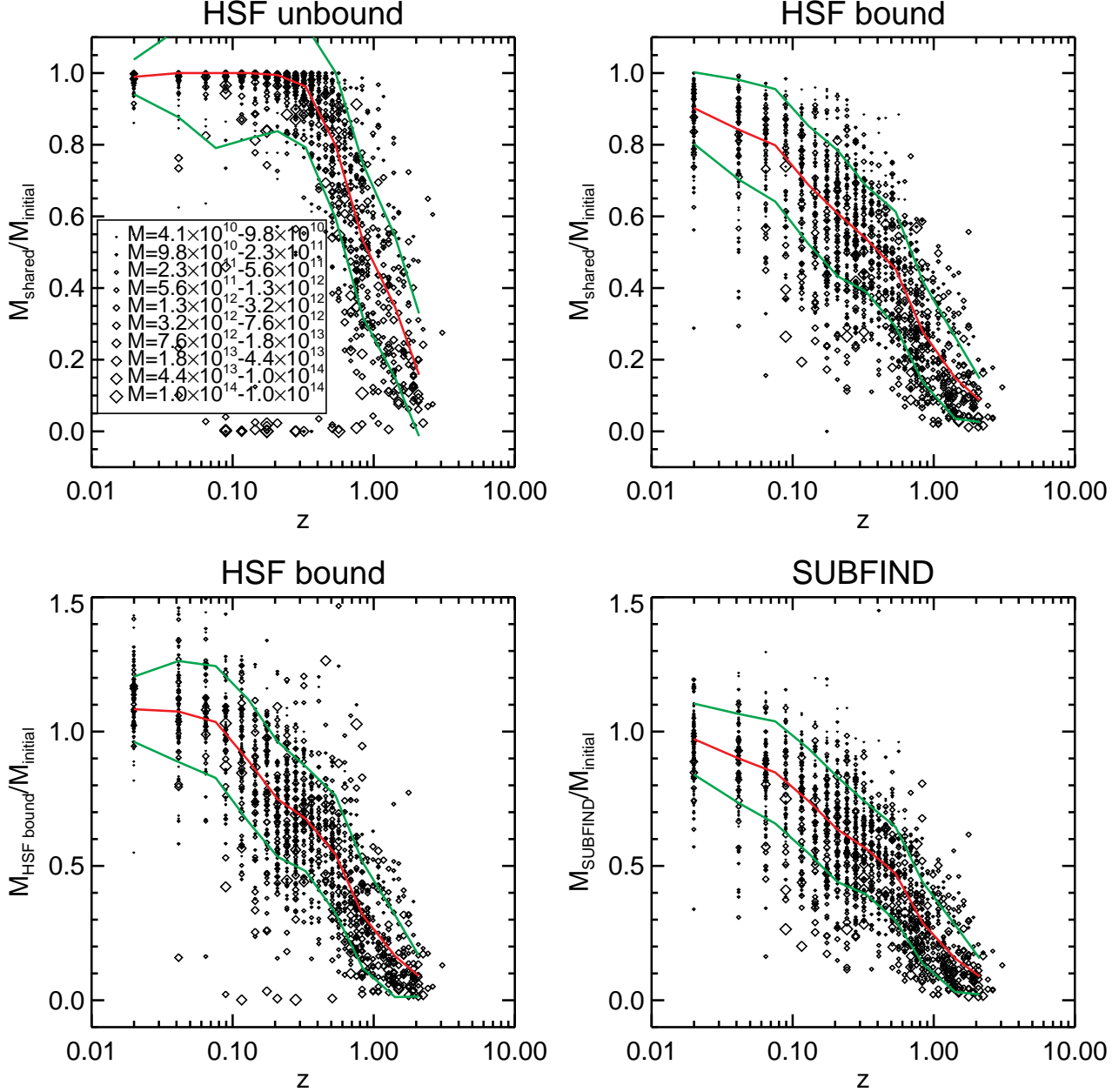
Figure 10. Mass loss of structures as a function of the redshift z of merging with the main halo. *Top-left panel:* the mass loss is presented as the ratio $M_{shared}/M_{initial}$, where M_{shared} is the mass in common between the HSF structure and its counterpart (of mass $M_{initial}$) just prior to merging with the main halo. *Top-right panel:* same as top left one, but for bound HSF structures. *Bottom-left and bottom-right panels:* same as the top ones, but the mass loss is presented as the ratio between total final mass and initial mass, for HSF bound structures and SUBFIND (bound) structures, respectively. On all the panels, the symbol size is proportional to $M_{initial}$. In addition we plot the median value (in red) and the σ errors calculated in 10 logarithmic bins (in green), with at least 10 structures per bin.

Keeping that in mind, we can now study the ratio $M_X/M_{initial}$ between the total mass of the identified bound structure and the mass of the initial halo as a function of redshift of merging, independently of whether the particles are shared between initial and final stage or not, as shown in the lower panels of Fig. 10 for HSF (X=HSF bound) and SUBFIND (X=SUBFIND). The results are not very different for both codes, except that, as already extensively argued previously, this ratio is slightly larger for HSF than for

SUBFIND. And because of the effect just discussed above (top left panel of Fig. 11), $M_X/M_{initial}$ can be larger than unity at low redshift.

While the correlation between the mass loss due to tidal stripping and the redshift of merging is quite obvious, the relationship between mass loss and initial mass is less evident, given the limited amount of statistical occurrences we analyse here (one single large cluster-sized Millennium halo). Figure 11 (right panel and bottom panels) indicates that the
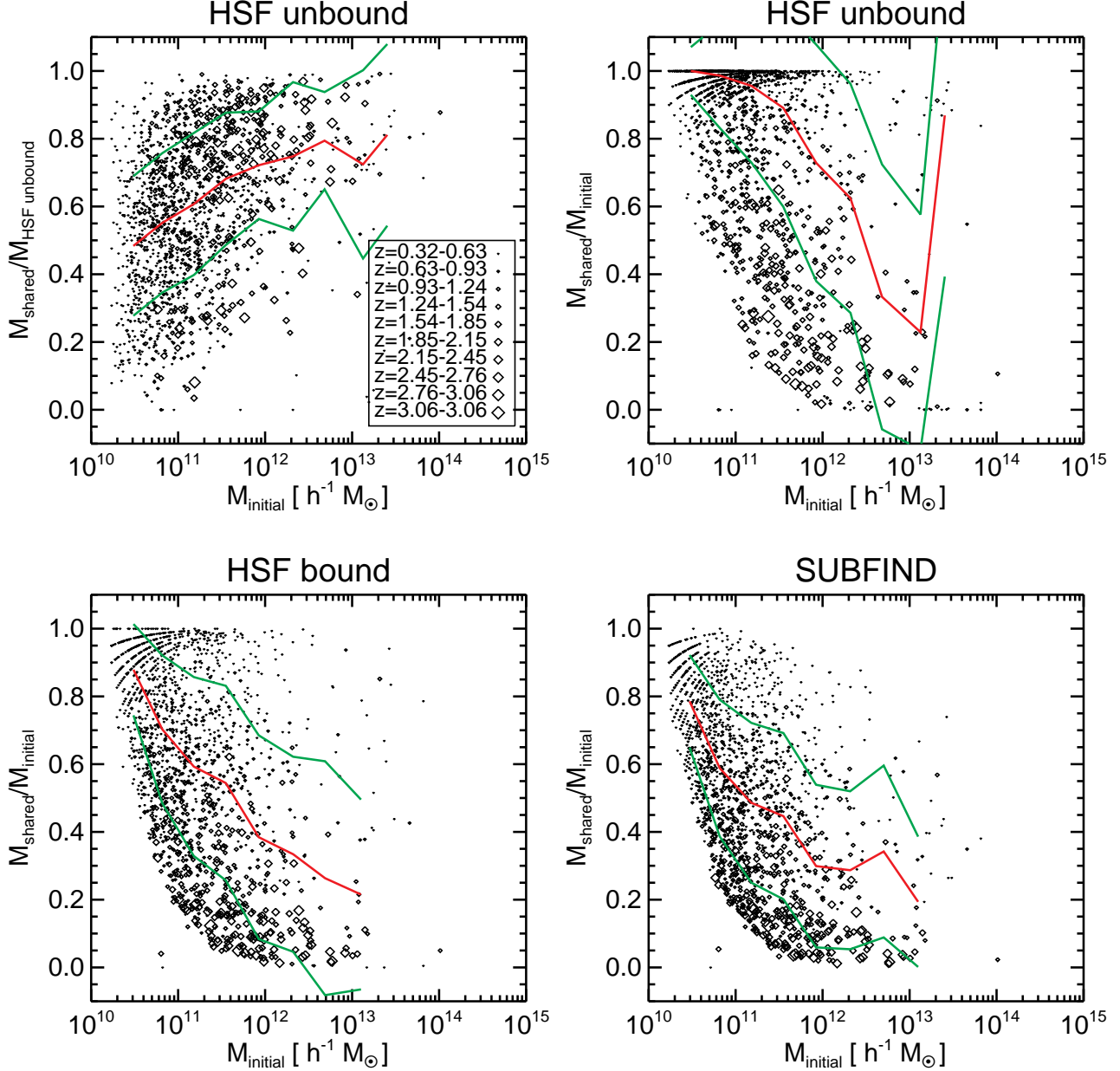
Figure 11. The mass, M_{shared}, in common between structures detected at present time by HSF and SUBFIND and their counterpart –of mass M_{initial}– just prior to merging with the main halo, is studied in a fractional way as a function of M_{initial}. *Top-left:* ratio between M_{shared} and the mass of the HSF unbound structure. *Top-right, bottom-left and bottom-right panel:* ratio between M_{shared} and M_{initial}, respectively for HSF unbound, HSF bound and SUBFIND structures. The symbol size is proportional to redshift z of merging with the main halo. In addition we plot the median values (in red) and the σ errors, calculated in 10 logarithmic bins (in green), with at least 10 structures per bin.

mass loss is significantly smaller for initially light structures than for initially massive ones. To demonstrate that unambiguously, we perform a more accurate analysis of the global mass loss displayed on the lower panels of Fig. 10, by fitting analytically the redshift and the mass dependence. To do so, we divide the initial mass of the structures into four logarithmic bins. Then for each bin, we fit the mass loss as a function of redshift in logarithmic coordinates (Figure 13) with the following convenient parametric form

$$\frac{M_{\mathrm{X}}}{M_{\mathrm{initial}}} = \frac{1}{(z/z_s)^{\eta}(1+z/z_s)^{\gamma}}. \qquad (2)$$

The best fitting parameters, found by a standard least-square method, are listed in Table 2. The fact that mass loss is more pronounced for more massive objects is clear, and was also to be expected. This behaviour can simply be explained as follows: small structures are more strongly bound, because they are more concentrated (e.g. Angulo et al. 2008), so they do not lose as much mass as large structures from tidal stripping. Indeed, the largest structures are less
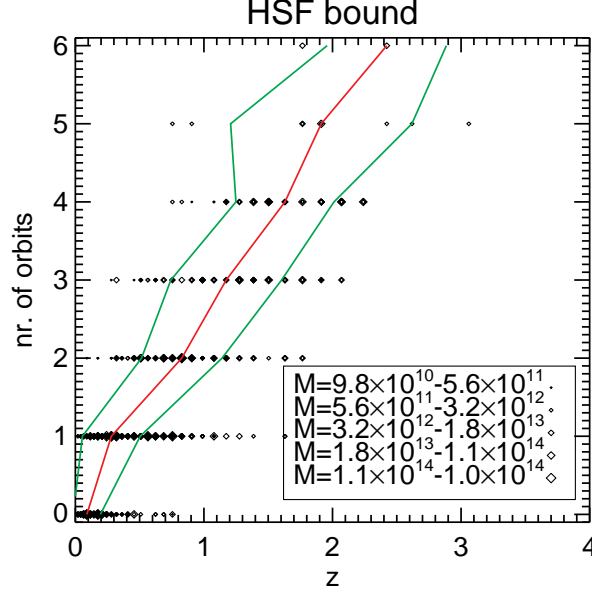
Figure 12. Number of orbits each structure made inside the main halo as a function of redshift of merging of the structure with the halo. The symbol size is proportional to M_{initial}, expressed in units of $M_{\odot}h^{-1}$. In addition, we plot the median value (in red) and the σ errors (in green) calculated in 10 logarithmic bins with at least 10 structures in each bin (for convenience, binning is performed on y axis). In our sample the structures do not made more than 6 orbits inside the main halo, before they disappear.

compact and are more sensitive to dynamical friction. As a result, they are strongly disrupted while they are orbiting around the main halo. They also tend to have more radial orbits.

4.3 Bound subhaloes, tidal tails and tidal streams

By studying the merger tree history, we could show that the HSF algorithm is capable of finding both substructures and their tidal tails. As we noticed, some of the tidal tails are still connected to their host substructures, while others are recognised as separate objects. We now study this bimodality more carefully.

To better separate tidal streams from the bound counterpart of substructures, we now take a small value of the connectivity parameter, $\alpha = 0.01$. In the following analysis, we shall study the five following populations:

(i) Bound substructures found by HSF;
(ii) Bound substructures found by SUBFIND;
(iii) All HSF substructures (before unbinding);
(iv) Unbound HSF structures: substructures found by HSF which disappear during the unbinding process, such as tidal streams;
(v) Bound HSF structures: substructures found by HSF (along with their tidal tails) which remain after the unbinding process.

To analyse substructures properties, we estimate, for each of them, the phase-space density maximum f_{max} and the minimum f_{min}. These 2 quantities are measured for the full set of particles belonging to the substructure prior to the unbinding process. To better measure high phase-space density

peaks, we use the SPH-AM EnBiD method with 32 neighbours.

In the top-right panel of Figure 14, the distribution of the f_{max} values of is shown. It is clearly bimodal, and this property is in fact independent of α. It is straightforward to understand the origin of the bimodality. The local phase-space density can for instance be approximated as follows (Maciejewski et al. 2008):

$$f(\mathbf{x}, \mathbf{v}) = \frac{\rho(\mathbf{x})}{(2\pi)^{3/2}\sigma^3(\mathbf{x})} \exp\left\{-\frac{[\mathbf{v} - \mathbf{v}_0(\mathbf{x})]^2}{2\sigma^2(\mathbf{x})}\right\}. \qquad (3)$$

Two cases can the be considered. In the centre of a bound substructure, i.e. a standalone structure that survived the unbinding process, the local density ρ is high and the local velocity dispersion $\sigma(\mathbf{x})$ is low, which gives a high local phase-space density maximum. On the other hand, when substructures are disrupted by strong tidal forces, their local density ρ decreases and their velocity dispersion, $\sigma(\mathbf{x})$, increases, so their peak phase-space density is lower.

These statements can be directly checked by unbinding the substructures found by HSF. On the top-right panel of Figure 14, the high density maxima peak of the distribution is dominated by the bound substructures, as expected. There is a small fraction of bound substructures for which f_{max} resides in the lower density maxima regime. We checked that this happens only for the smallest substructures with around 20 particles, for which Poisson noise fluctuations start to be significant. The lower peak of the distribution of values of f_{max} is mainly occupied by unbound substructures. There are still some unbound substructures residing in the higher peak. They have less than 100 particles and can be considered as "Poisson clusters" (even in Poisson noise it is possible to find high density contrasts).

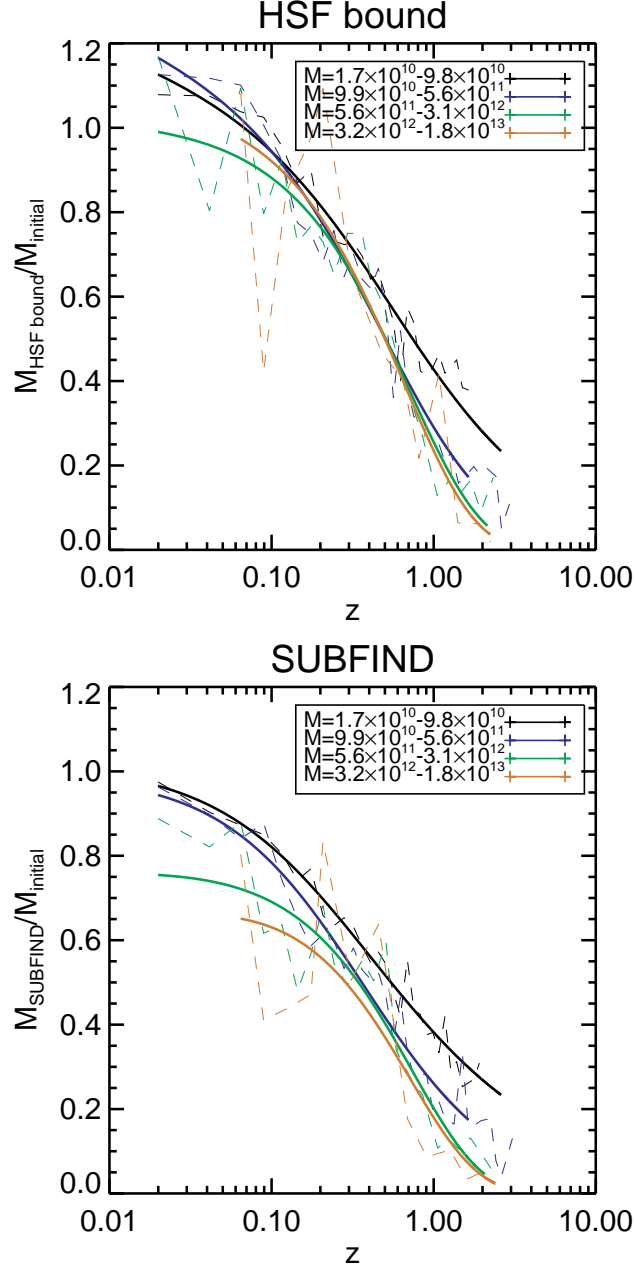Note that the high f_{max} distribution peak is very sharp,

Figure 13. Mass loss as a function of redshift of merging z for masses binned in 4 logarithmic bins (dotted curves) with its smooth fit given by equation (2) (thick curves). For each dotted curve, the number of bins is equal to $2\sqrt{N}$, where N is the number of samples. These two panels are equivalent to bottom panels of Fig. 10. To make adequate fitting, we perform Levenberg-Marquardt least-square minimisation with sigma errors set from Poisson noise counting distribution. Masses are expressed in units of $M_\odot h^{-1}$.

Table 2. Parameters used in Eq. (2) to fit results presented in Figure 13.

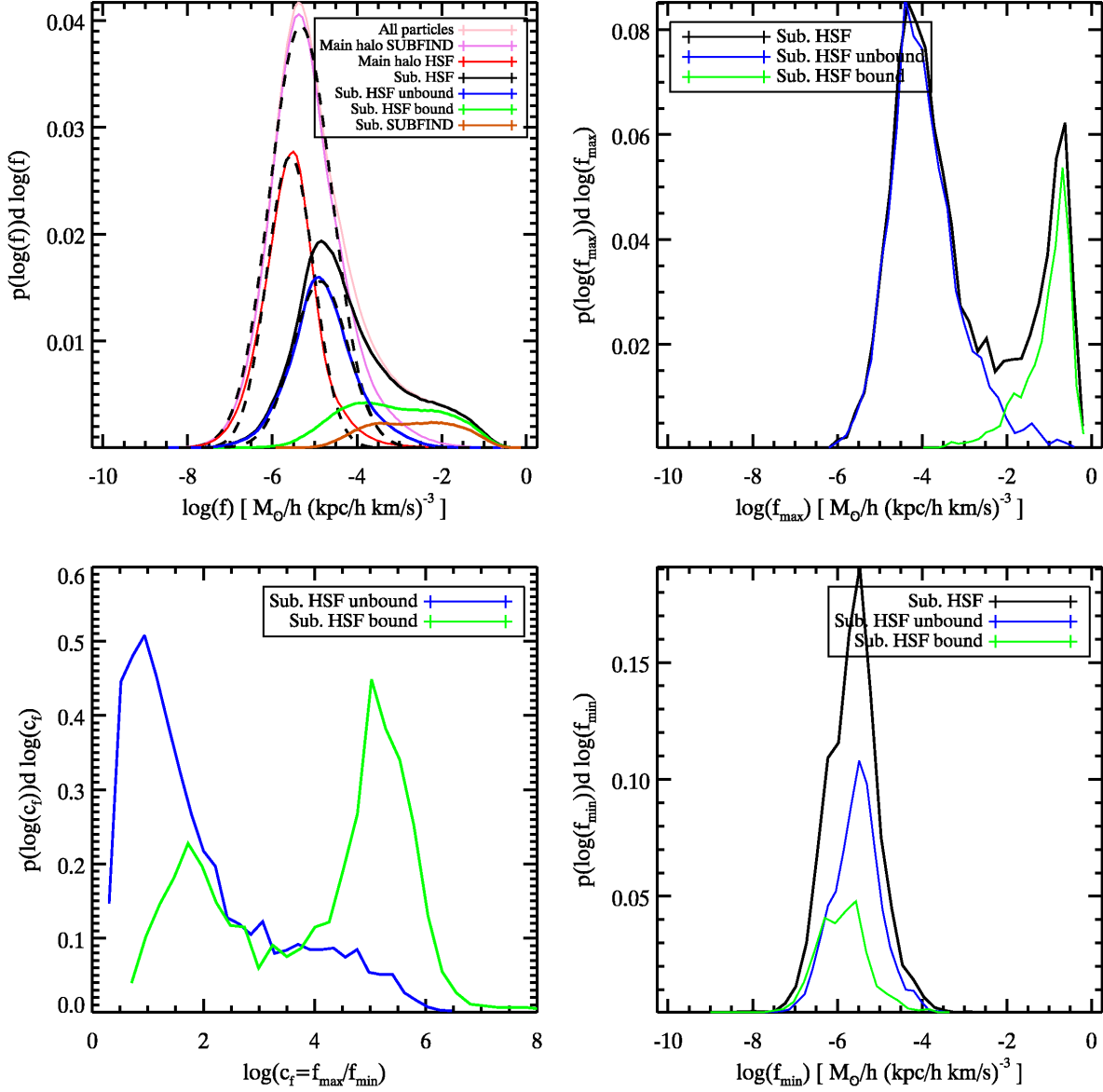| mass min	mass max	HSF x_s	HSF η	HSF γ	SUBFIND x_s	SUBFIND η	SUBFIND γ
1.7×10^{10}	9.8×10^{10}	0.54	0.04	0.78	0.30	-0.00	0.66
9.9×10^{10}	5.6×10^{11}	1.02	0.05	1.82	0.40	0.00	1.06
5.6×10^{11}	3.1×10^{12}	20.11	0.00	28.31	1.46	-0.03	3.01
3.2×10^{12}	1.8×10^{13}	19188.89	0.01	28851.01	18.93	-0.07	25.61

Figure 14. Disentangling tidal streams from bound substructures: phase-space density distributions. *Top-left*: distribution function of logarithm of phase-space density f estimated for all particles belonging to each category of substructures as indicated inside the panel (100 logarithmic bins). The black dashed lines represent the best fitted Gaussian functions for the main halo found by SUBFIND, the main halo found by HSF and the unbound structures found by HSF (including the tidal tails of bound structures). This means in fact that for each of these components, f is lognormal if the fit is good. To make adequate fitting, we perform Levenberg-Marquardt least-square minimisation with sigma errors set from Poisson Noise counting distribution. *Top-right, bottom-right*: distribution function of substructures maxima, f_{max}, and minima, f_{min} (50 logarithmic bins). The substructures are separated into unbound components (blue) and bound ones (green), while the black curve corresponds to all the substructures. *Bottom-left*: distribution function of substructures phase-space "peakness", defined as $c_f = f_{max}/f_{min}$.

Table 3. For each substructure we measure its maximum phase-space density f_{max}, minimal value f_{min}, maximum 3D density ρ_{max}, minimum one ρ_{min}, its phase-space density "peakness", $c_f = f_{max}/f_{min}$, and 3D density "peakness", $c_\rho = \rho_{max}/\rho_{min}$. Phase-space density is quoted in $M_\odot h^2 \text{kpc}^{-3} \text{km}^{-3} \text{s}^3$, while ρ is expressed in units of total average density $\langle \rho \rangle$.

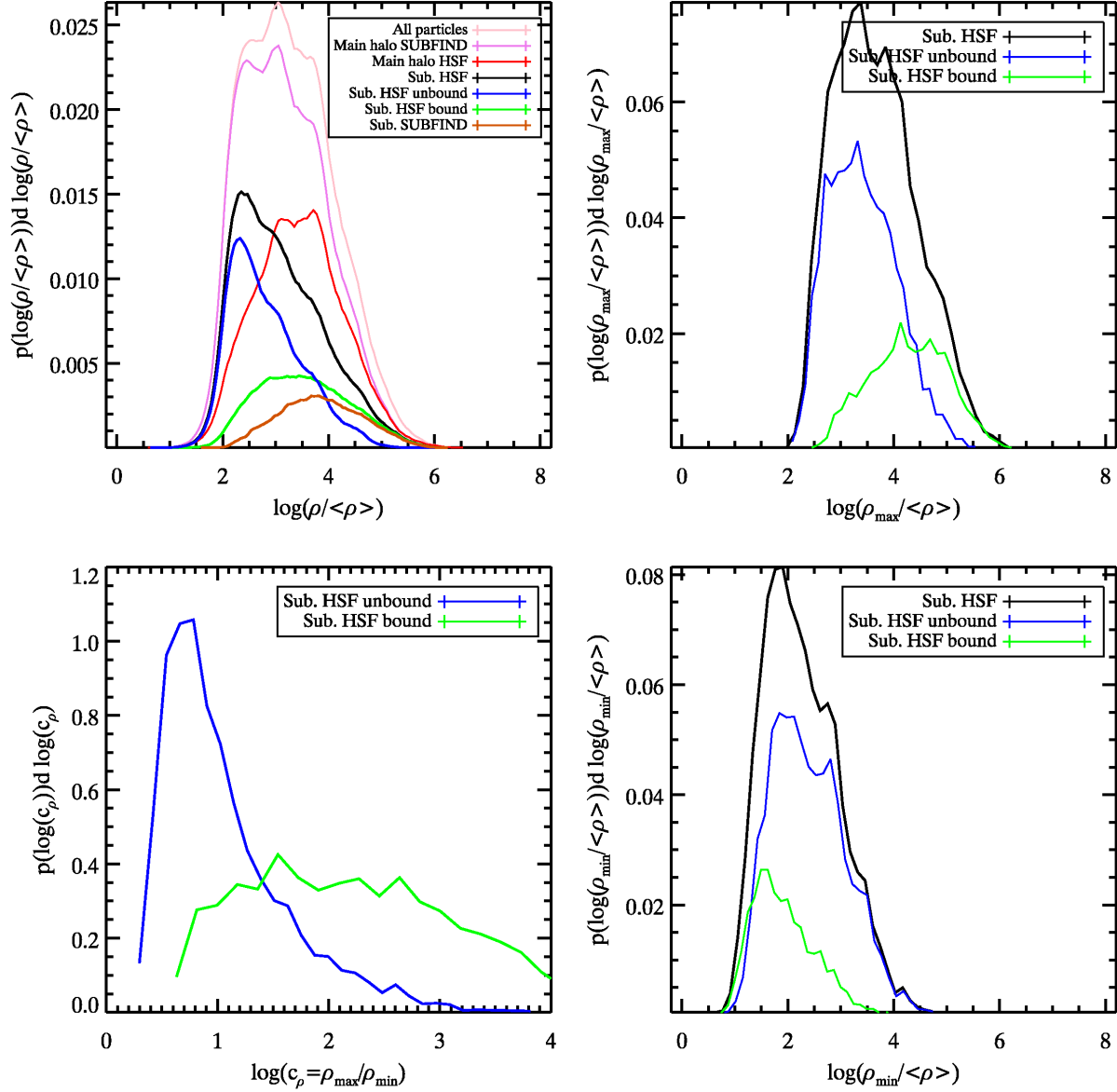| Structure class	f_{max}	f_{min}	c_f	ρ_{max}	ρ_{min}	c_ρ
HSF unbound	4.0×10^{-5}	3.3×10^{-6}	8.7	2.1×10^3	69.2	6.1
HSF bound	0.2	2.7×10^{-6}	1.1×10^5	1.4×10^4	31.2	35.5

Figure 15. Disentangling tidal streams from bound substructures: projected 3D density distributions. *Top-left*: distribution function of normalised density $1 + \delta = \rho/\langle\rho\rangle$ estimated for all particles belonging to each category of substructures as indicated on the panel (100 logarithmic bins). *Top-right, bottom-right:* distribution function of substructure maxima $\rho_{\max}/\langle\rho\rangle$, minima $\rho_{\min}/\langle\rho\rangle$ (50 logarithmic bins); *bottom-left:* distribution function of substructures density "peakness" defined as $c_\rho = \rho_{\max}/\rho_{\min}$.

corresponding to $f_{\max} \simeq 0.2 M_\odot h^2 \mathrm{kpc}^{-3}\mathrm{km}^{-3}\mathrm{s}^3$. As already noticed in Maciejewski et al. (2008), all the bound substructures present approximately the same value of $f_{\max}$ (see also Vass et al. 2008). This property could be simply an upper bound imposed by numerical resolution or set by the dynamics, or more likely a combination of both (e.g., Binney 2004; Vass et al. 2008). The second peak, dominated by tidal streams, is less pronounced, although still quite well defined, with a maximum at $f_{\max} \simeq 4.0 \times 10^{-5} M_\odot h^2 \mathrm{kpc}^{-3}\mathrm{km}^{-3}\mathrm{s}^3$, a value about 3.7 orders of magnitude lower than what is found for bound structures (all the values are summarised in table 3). This shows again the very clear separation between bound structures and tidal streams.

Another way of separating various substructure popula-

tions consists of measuring their "peakness", i.e. the parameter $c_f = f_{\max}/f_{\min}$, where $f_{\min}$ is the minimum value of the phase-space distribution function of the HSF structures (prior to unbinding). The advantage of the peakness parameter is that, as opposed to $f_{\max}$, it does not depend on a specific choice of units: a structure with a bound component should present a peakness parameter very large compared to unity, contrary to a pure tidal stream. The measurement of c_f is however meaningful only if $f_{\min}$ is well defined. This is *a priori* not obvious as one expects $f_{\min}$ to be very sensitive to local fluctuations in the noise, which indeed affect the local topology strongly. We checked that in fact $f_{\min}$ is a robust statistics, as suggested by the rather symmetric behaviour of the curves shown in the bottom-right panel of Figure 14.

Table 4. Mass in each substructure class compared to the total mass in our Millennium test halo.

Structure class	mass
SUBFIND bound	12.4%
HSF bound	18.8%
HSF unbound $\alpha = 0.2$	22.5%
HSF unbound $\alpha = 0.01$	31.6%
HSF $\alpha = 0.2$	41.2%
HSF $\alpha = 0.01$	50.4%

Table 5. Best parameters of the Gaussians fitted to the distribution function of the logarithm of phase-space density estimated for all particles belonging to each category of substructures (top-left panel of Figure 14).

Structure class	mean	σ	χ^2 error
SUBFIND main halo	4.7×10^{-6}	0.73	7.39
HSF main halo	2.7×10^{-6}	0.55	1.11
HSF unbound substructures	1.4×10^{-5}	0.65	0.34

The distribution of measured values of c_f is shown in the bottom-left panel, and presents of course the same bimodal nature as $f_{\max}$. For instance, one finds that c_f is typically of the order of 10^5 for bound structures, while it is only of the order of 10 for tidal streams.

Finally, the top-left panel shows the distribution of measured values of f for each dark matter particle. In this plot, particles left over after unbinding HSF substructures, i.e. belonging to the tidal tails of these substructures, are put on the list of unbound substructures. The high phase-space density region is dominated by bound substructures, which is consistent with the observations we made for the $f_{\max}$ distribution function. Note that HSF bound substructures are more extended into lower phase-space density regions than SUBFIND ones and are more likely to overlap in terms of density with unbound streams. There is in total almost 19% of mass in HSF bound substructures to compare with 12.4% in SUBFIND ones (see Table 4). This additional mass in HSF bound substructures comes from particles which were not found with the saddle point algorithm working in 3D position space on which SUBFIND is based. This means that the total bound mass of substructures strongly depends on the cutting criterion applied to the 3D density field ρ, even with the additional unbinding procedure.

An examination of the top left panel of Figure 14 suggests that it is possible to perform an optimal cut on f, with a value chosen between 3×10^{-5} and $3 \times 10^{-4}\,M_\odot h^2 \text{kpc}^{-3}\text{km}^{-3}\text{s}^3$ so that most particles with phase-space density above this threshold belong to bound substructures. Such a criterion was used before in the literature to mark substructures (Stadel et al. 2008). Tidal streams and possibly signatures of caustics occupy the middle range of phase-space densities, with 31.6% (22.5% for $\alpha = 0.2$) of the total FOF halo mass belonging to them, which is more than for bound substructures. Similarly as for bound substructures, we can set some lower limit around 10^{-5} on the phase-space density and claim that most particles with higher value of f than this limit belong to substructures of some kind (bound or unbound). The low phase-space density regime is indeed dominated by the main halo component.

As a final note on the upper-left panel of Figure 14, we found that the shape of the distribution function of values f observed for each component has interesting properties: it is very well fit by a lognormal distribution both for the main halo component found by SUBFIND and HSF, and the unbound substructures found by HSF. This complements the findings of Vass et al. (2008), who performed a similar analysis but used a more *add-hoc* approach to separate various components contributing to the phase-space distribution

function. The best fitting parameters of a Gaussian on the logarithm of f are given in Table 5. The interpretation of these results did not seam straightforward to us, so we decided to leave it for future work. Certainly, a path to follow is to examine the arguments developed by Coles & Jones (1991) to explain the close to lognormal behaviour of the projected 3D density, ρ, relying on the continuity equation and the positivity of the density.

In practice, in observations of, e.g., X-rays clusters or gravitational lensing, the 3D density ρ (or its projection on the sky) is usually used to model dark matter haloes instead of the phase-space density f. To illustrate how the previous results translate in terms of ρ, Figure 15 is similar to Figure 14, but the calculations are performed for the normalised density $1 + \delta = \rho/\langle\rho\rangle$ instead of f. The 3D density is measured using EnBiD's SPH kernel with 32 neighbours. Contrary to Figure 14, the distribution function of values of $\rho_{\max}$ (upper right panel) shows only one peak. The difference between bound and unbound structures shows much less contrast (see Table 3 for numerical estimates of typical values of $\rho_{\max}$, $\rho_{\min}$ and $c_\rho \equiv \rho_{\max}/\rho_{\min}$). In particular, bound structures present a large spread on their 3D local density maxima of about 2 orders of magnitudes, in contrast with what happens with $f_{\max}$, and they are more difficult to disentangle from their unbound counterpart, even with the peakness, c_ρ, although this latter quantity seems to have a better separating power than $\rho_{\max}$ (lower left panel).

Interestingly, the particle density distribution diagram (top-left panel of Figure 15) is populated in a different way from what happens in phase-space. In particular, tidal streams occupy the low density region although they still spread over a large dynamic range, while the main halo dominates the high density regime. Bound substructures are rather subdominant and spread over the whole dynamic range.

To complete this section, Figure 16 and Figure 17 show the appearance of bound structures, unbound ones, and of the smooth part of the halo after removal of all HSF structures. There is a subtle but significant difference between the two figures. In Figure 16, the top panels show only the bound part of the bound substructures, while the top panels of Figure 17 show the bound structures along with their tidal tails. In the middle panels of Figure 16, particles both belonging to unbound structures and particles removed from the bound structures during the unbinding process are shown. In contrast, the bottom panels of Figure 17 show only particles belonging to unbound structures. This results in an asymmetry in middle right panel of Figure 16, which reflects the fact that structures passed through (or nearby) the centre of the halo one more time in the upper part of the phase-space
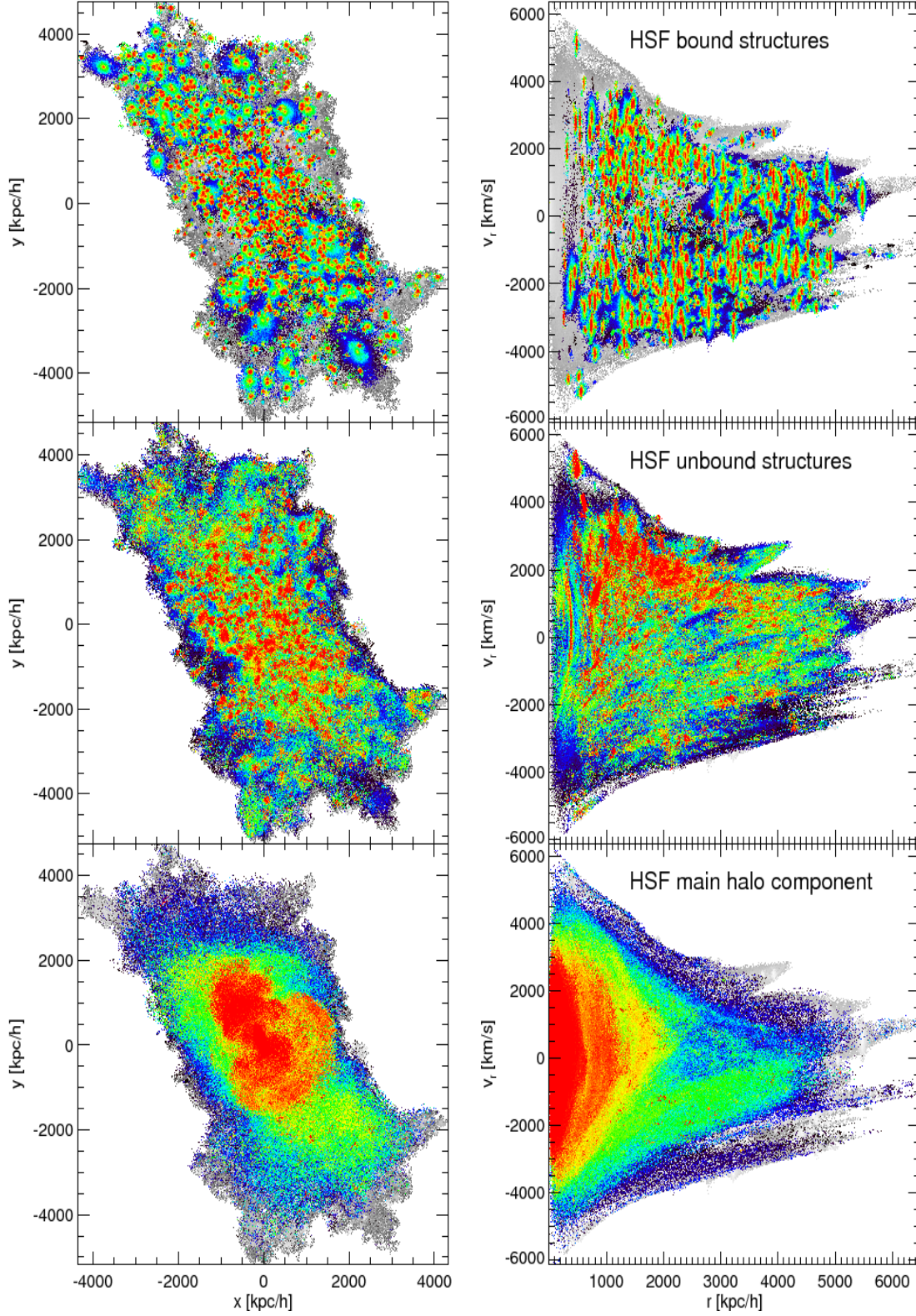
Figure 16. Appearance of bound and unbound structures in our Millennium test halo. *Top panels:* particles belonging to HSF bound structures (so unbound particles are removed). *Middle panels:* particles which belong to HSF unbound substructures or are left over in the tails of HSF bound substructures after the unbinding process. *Bottom panels:* the main halo after removal of all substructures. From left to right: x–y position space, radius r–radial velocity v_r phase-space. The pictures are computed in 3 steps as follows: (i) division of space into a three-dimensional equally spaced grid with $N = 400$ divisions across each x, y, z axes, (ii) calculation of the mean density f of all particles inside each cell and (iii) projection of this density on the $x - y$ plane by taking in each z column the cell with the highest density. To enhance the contrasts, equalisation of the histograms in $\log f$ was implemented.
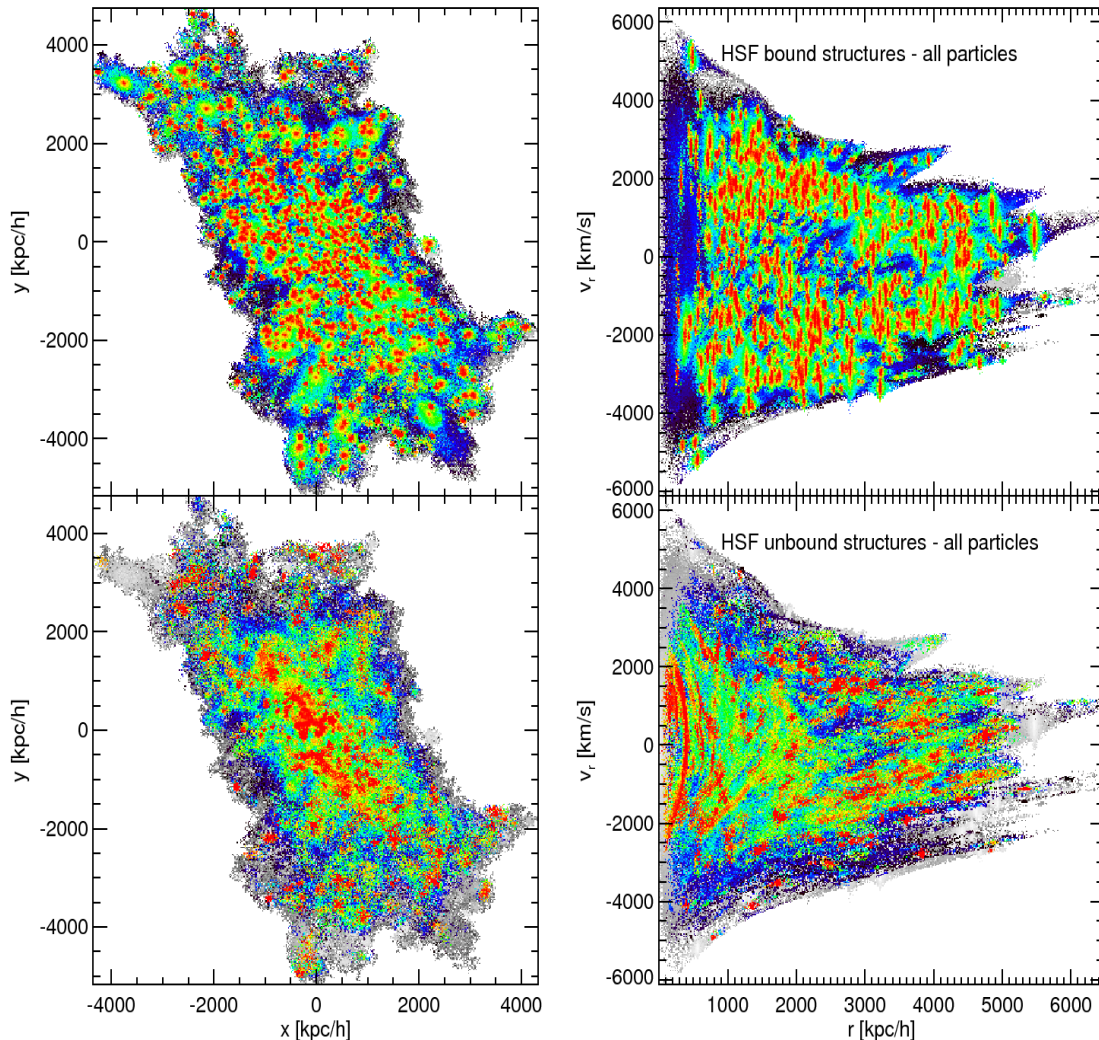
Figure 17. Same as Figure 16, but the set up is slightly different: in the *top panels*, the HSF structures which are seeds of bound structures are displayed entirely, including their tidal tails. In the *bottom panels,* only HSF structures which are unbound are displayed.

diagram than in the lower part. Tidal disruption is indeed more significant and thus removes particles with higher value of f in the upper part of the phase-space diagram than in the lower part. Not surprisingly, the asymmetry disappears in the bottom right panel of Figure 17. Note that bound structures are absent in the region close to the main halo centre, as expected. Note as well the rather elongated tidal streams, in particular close to the halo centre, in the bottom right panel of Figure 17 and the middle right panel of Figure 16. These are the left overs of structures disrupted by strong tidal forces. In the bottom right panel of Figure 16, the main halo still presents, after cleaning, some filamentary structures, which are parts of tidal tails, or less likely, signatures of caustics. It can be cleaned even more by using a smaller value of the connectivity parameter α.

5   DISCUSSIONS AND CONCLUSIONS

We introduced a new universal multi-dimensional hierarchical structure finder (HSF) which was employed here to study

dark matter structures in six dimensional phase-space. The algorithm used, for each particle, the phase-space density and local neighbourhood estimated with the SPH method with adaptive metric implemented in the EnBiD package (Sharma and Steinmetz 2005). To detect structures, HSF builds on the SUBFIND and ADAPTAHOP algorithms, with the introduction of a new simple but robust cut or grow criterion depending on a single connectivity parameter α.

The main steps of the algorithm are as follows: (i) local phase-space density maxima are detected and structures around them are grown by following local gradients up to saddle points; (ii) at each saddle point level, the density f of each structure is compared to Poisson noise: the structure is kept if f is β times more significant than the Poisson r.m.s. noise level. At the same time its mass and the mass of its partner (connected to it through the saddle point) are measured and the cut or grow criterion is applied: if one structure is α times smaller than its neighbour, then all particles below the saddle point are attached to the neighbour. When the two structures have comparable mass within a factor α,

they are both set to grow down as before. This criterion allows us to better trace substructures in phase-space, with a good control of the effect of Poisson noise, which is very important in this rather sparsely sampled space.

We demonstrated the potential of HSF on a large FOF dark matter halo taken from the Millennium Simulation. Our tests show that β and especially α are important control parameters. To better study the smallest possible structures, β should be set close to 0. The smaller α, the more subtle the structures found by the algorithm. In our analysis, we give preference to $\alpha = 0.2$, which provides a good balance between finding the finest possible substructures and not overgrowing them. This value of α is particularly appropriate when an additional binding step is performed. In contrast, an analysis of tidal tails is best carried out with small α, around $0.01 - 0.001$, which separates structures into smaller pieces. It is possible to use it in combination with $\beta = 4 - 10$, which tends to reconnect the structures together in a consistent way, to reconstruct tidal tails rather well. A more advanced method of reconnecting phase-space structures, by using the topology of the hierarchical tree created by the HSF algorithm is under investigation.

We used the Millennium Simulation merger tree (Springel et al. 2005b) to compare the HSF phase-space structures found at the present time with the same structures traced back to the time just before they enter the main halo. While the best three dimensional algorithms used presently, such as SUBFIND, manage to find only the main part of bound structures, HSF is capable of finding more extended bound components along with their tidal tails. There is much more information about structure evolution still stored in phase-space than in 3D and this information can be potentially fully recovered from the data by a six dimensional algorithm such as HSF.

The main results of our analysis in time and space domain are the following:

• HSF structures contain on average $80 - 100\%$ of the mass inside the initial structures up to a redshift of merging $z = 0.3 - 0.4$. This value drops down to 50% for $z = 1$. On the other hand, bound HSF structures contain on average $80 - 100\%$ of the mass inside the initial halos only up to $z = 0.09$ and 50% up to $z = 0.6$. This shift in the mass loss is caused by the existence of tidal tails, which are joined to HSF structures, but do not belong to their bound part. In other words we can say that HSF is able to reconstruct in most cases the full dynamical structures which enter the halo at redshifts as high as $z = 0.3 - 0.4$.

• The distribution function of the phase-space density maxima f_{max} of HSF structures clearly shows a bimodality. We can explain it by partitioning the structures into two distinct groups. In the first group, corresponding to the high phase-space density peak regime, $f_{max} \approx 0.2 M_\odot h^2 \mathrm{kpc}^{-3} \mathrm{km}^{-3} \mathrm{s}^3$, with a small spread around that value, there are mostly bound structures. In the second group, corresponding to a 3 orders of magnitude smaller phase-space density regime, $f_{max} \approx 3.3 \times 10^{-5} M_\odot h^2 \mathrm{kpc}^{-3} \mathrm{km}^{-3} \mathrm{s}^3$, and a larger spread around this value, there are all unbound structures i.e. tidal tails, streams and possibly some caustics. In terms of "peakness", $c_f = f_{max}/f_{min}$, where f_{min} is minimum value of f in each
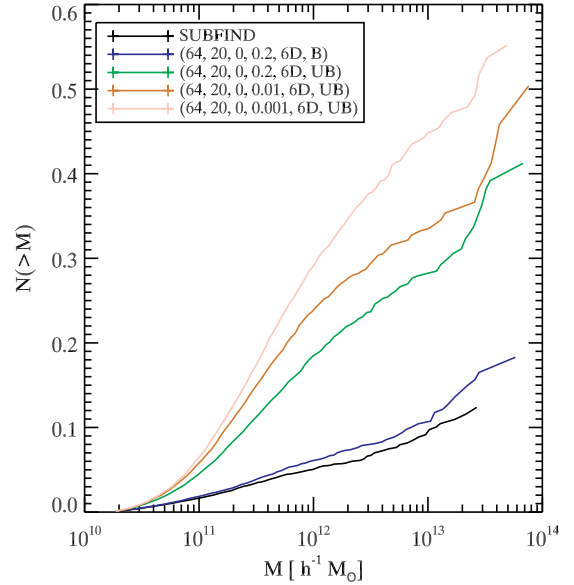

Figure 18. Cumulative mass in substructures found by SUBFIND, bound HSF method, and HSF with different choices of the connectivity parameter α.

substructure, this translates into $c_f = 1.1 \times 10^5, 8.7$ for bound and unbound structures, respectively.

• We noticed, similarly as Vass et al. (2008), that the distribution function of the values of f around each dark matter particle is close to lognormal for the smooth component of the halo and the unbound part of the substructures (tidal streams).

• We found that there is more mass in bound HSF substructures than in SUBFIND ones. Figure 18 shows the cumulative mass of substructures divided by the total halo mass as a function of substructure mass. Around 18.5% of halo mass is stored in bound HSF structures, and this quantity almost does not depend on α. In comparison, about 12.4% of the mass is stored in SUBFIND bound structures. The additional mass in HSF bound structures comes mainly from the fact that subhaloes are better defined in phase-space and are more extended. However, the set of identified bound substructures is nearly identical in both methods, and hence the cumulative abundance of substructures as a function of maximum circular velocity is the same as well.

We note that in our test halo, 41.2% of the mass belongs to substructures for $\alpha = 0.2$, 50.4% for $\alpha = 0.01$, and 55.2% for $\alpha = 0.001$. When we substract from these numbers the contribution of bound structures, we find that $22.9\% - 36.4\%$ of halo mass is stored in unbound structures. This should be taken into account when analytical models of halos with substructures are proposed.

• While we would need a larger statistical sample of halos to perform robust measurements, we noticed that at fixed redshift of merging with the main halo, small structures tend to lose less mass than larger ones, in agreement with expectations based on the higher concentration of smaller halos. Also, we found a strong correlation between mass loss and the number of orbits a substructure can make inside the main halo.

When we observe our own Galaxy, we do not have access to different "snapshots" anymore, in stark difference with the world of simulations. Instead, we have to be content with the data at the present time. However, because we now know that our phase-space structure finder can identify dynamical structures that were bound before tidal disruption, it can provide totally new insights about the past dynamical history of our Galaxy. Within the hierarchical framework, we expect that our Galaxy should be made through the merging of more than about 100 smaller subcomponents. Comparing structures in observational data and simulations can be one of the best tests for the theory of hierarchical galaxy formation, and provide important constraints on cosmological models such as ΛCDM.

Up to now, we studied only the evolution of dark matter, but we can also similarly study the evolution of baryons in gas and stars. Galaxies are observed in many different ways, ranging from star distributions, velocity and chemical properties, to HI measurements, etc. Our phase-space structure finder with local metric fitting is in fact implemented in such a way that it can be used in any number of dimensions, where each dimension can have completely different physical units. So it is in principle straightforward to use it for studying galaxy structure evolution in multi-dimensional space with the appropriate probabilistic weightings to take into account the noise and holes (missing measurements) in the data hypercube. We think that such an approach can yield a deeper understanding of galaxy evolution, and looks especially promising in light of the upcoming GAIA mission (Gilmore et al. 1998) which plans to map the positions of around one billion stars in our Galaxy.

ACKNOWLEDGMENTS

REFERENCES

Angulo R. E., Lacey C. G., Baugh C. M., Frenk C. S., 2008, arXiv:0810.2177

Alard C., Colombi, S., 2005, MNRAS, 359, 123

Aubert D., Pichon C., Colombi S., 2004, MNRAS, 352, 376A

Bertschinger E., 1985, ApJS, 58, 39

Binney J., 2004, MNRAS, 350, 939B

Cole S., Lacey C., 1996, MNRAS, 281, 716

Coles P., Jones B., 1991, MNRAS, 248, 1

Colombi S., Touma J., 2007, CNSNS, 03, 012

Davis M., Efstathiou G., Frenk C. S., White S. D. M., 1985, ApJ, 292, 371

Diemand J., Kuhlen M., Madau P., 2006, ApJ, 649, 1

Eisenstein D. J., Hut P., 1998, ApJ, 498, 137

Gelb J., Bertschinger E., 1994, ApJ, 436, 467

Gilmore G. F., Perryman M. A., Lindegren L., Favata F., Hoeg E., et al., 1998, SPIE, 3350, 541G

Governato F., Moore B., Cen R., Stadel J., Lake G., Quinn T., 1997, NewA, 2, 91

Hinshaw G., Weiland J. L., Hill R. S., Odegard N., Larson D., Bennett C. L. et al., 2008, arXiv:0803.0732

Kim J. & Park, C., 2006, ApJ, 639, 600

Klypin A., Gottlober S., Kravtsov A. V., Khokhlov, A. M., 1999, ApJ, 516, 530

Lacey C., Cole S., 1994, MNRAS, 271, 676

Lukić Z., Reed D., Habib S., Heitmann K., 2008, arXiv:0803.3624

Maciejewski M., Colombi S., Alard C., Bouchet F., Pichon C., 2008, MNRAS, in press (arXiv:0810.0504)

Massey R., Rhodes J., Ellis R., Scoville N., Leauthaud A. et al., 2007, Nature, 445, 286M

Mohayaee R., Salati P., 2008, arXiv:0801.3271

Natarajan P., De Lucia G., Springel V., 2007, MNRAS, 376, 180

Navarro J. F., Frenk C. S., White S. D. M., 1997, ApJ, 490, 493

Neyrinck M. C., Gnedin N. Y., Hamilton A. J. S., 2005, MNRAS, 356, 1222

Rubin V. C., Ford. W. K. J., 1970, ApJ, 159, 379

Sharma, S., Steinmetz, M., 2006, MNRAS 373, 1293

Springel V., White S. D. M., Tormen G., Kauffmann G., 2001, MNRAS, 328, 726

Springel V., White S. D. M., Jenkins A., Frenk, C. S., et al., 2005a, Nature, 435, 629

Springel V., White S. D. M., Jenkins A., Frenk, C. S., et al., 2005b, Nature, 435, 629, Supplementary Information (astro-ph/0504097v2)

Springel V., 2005, MNRAS, 364, 1105

Springel V., White S. D. M., Frenk C. S., Navarro J. F., Jenkins, A., et al., 2008, arXiv:0809.0894

Stadel J., Potter D., Moore B. Diemand, J., Madau P. et al. astro-ph/0808.2981v2

Van Waerbeke, L., Mellier Y., Erben T., Cuillandre J. C., Bernardeau F. et al., 2000, A&A, 358, 30

Vass H.M., Valluri M., Kravtsov A.V., Kazantzidis S., 2008, submitted to MNRAS (arXiv:0810.0277)

Vogelsberger M., White S.D.M., Helmi A., Springel V., 2008, MNRAS, 385, 236

White S. D. M., Rees M. J., 1978, MNRAS, 183, 341

White S.D.M., Vogelsberger M., 2008, arXiv:0809.0497

Zwicky F., 1933, Helvetica Physica Acta, 6, 110